HAL
open science

Concentrations of OH and HO2 radicals during NAMBLEX: measurements and steady state analysis

S. C. Smith, J. D. Lee, W. J. Bloss, G. P. Johnson, D. E. Heard

To cite this version:

S. C. Smith, J. D. Lee, W. J. Bloss, G. P. Johnson, D. E. Heard. Concentrations of OH and HO2 radicals during NAMBLEX: measurements and steady state analysis. Atmospheric Chemistry and Physics Discussions, 2005, 5 (6), pp.12403-12464. hal-00301964

HAL Id: hal-00301964

https://hal.science/hal-00301964v1

Submitted on 18 Jun 2008

HAL is a multi-disciplinary open access archive for the deposit and dissemination of scientific research documents, whether they are published or not. The documents may come from teaching and research institutions in France or abroad, or from public or private research centers.

L'archive ouverte pluridisciplinaire **HAL**, est destinée au dépôt et à la diffusion de documents scientifiques de niveau recherche, publiés ou non, émanant des établissements d'enseignement et de recherche français ou étrangers, des laboratoires publics ou privés.

Atmos. Chem. Phys. Discuss., 5, 12403–12464, 2005
www.atmos-chem-phys.org/acpd/5/12403/
SRef-ID: 1680-7375/acpd/2005-5-12403
European Geosciences Union

Atmospheric Chemistry and Physics Discussions

Concentrations of OH and HO_2 radicals during NAMBLEX: measurements and steady state analysis

S. C. Smith[1], J. D. Lee[2], W. J. Bloss[1], G. P. Johnson[1], and D. E. Heard[1]

[1]School of Chemistry, University of Leeds, Leeds, LS2 9JT, UK
[2]Department of Chemistry, University of York, Heslington, York, YO10 5DD, UK

Received: 19 September 2005 – Accepted: 1 October 2005 – Published: 28 November 2005

Correspondence to: D. E. Heard (d.e.heard@leeds.ac.uk)

© 2005 Author(s). This work is licensed under a Creative Commons License.

Abstract

OH and HO_2 concentrations were measured simultaneously at the Mace Head Atmospheric Research Station in the summer of 2002 during the NAMBLEX (North Atlantic Marine Boundary Layer EXperiment) field campaign. OH was measured by laser-induced fluorescence employing the FAGE (Fluorescence Assay by Gas Expansion) technique, with a mean daytime detection limit of 2.7×10^5 molecule cm^{-3} (5 min acquisition period; signal-to-noise ratio = 1). HO_2 was detected as OH following its chemical conversion through addition of NO, with a mean detection limit of 4.4×10^6 molecule cm^{-3}. The diurnal variation of OH was measured on 24 days, and that of HO_2 on 17 days. The local solar noon OH concentrations ranged between $(3–8)\times10^6$ molecule cm^{-3}, with a 24 h mean concentration of 9.1×10^5 molecule cm^{-3}. The local solar noon HO_2 concentrations were $(0.9–2.1)\times10^8$ molecule cm^{-3} (3.5–8.2 pptv), with a 24 h mean concentration of 4.2×10^7 molecule cm^{-3}. HO_2 radicals in the range $(2–3)\times10^7$ molecule cm^{-3} were observed at night. During NAMBLEX, a comprehensive suite of supporting measurements enabled a detailed study of the behaviour of HO_x radicals under primarily clean marine conditions. Case study periods highlight the typical radical levels observed under different conditions. Steady state expressions are used to calculate OH and HO_2 concentrations and to evaluate the effect of different free-radical sources and sinks. The diurnally averaged calculated to measured OH ratio was 1.04±0.36, but the ratio displays a distinct diurnal variation, being less than 1 during the early morning and late afternoon/evening, and greater than 1 in the middle of the day. For HO_2 there was an overprediction, with the agreement between calculated and measured concentrations improved by including reaction with measured IO and BrO radicals and uptake to aerosols. Increasing the concentration of IO radicals included in the calculations to above that measured by a DOAS instrument with an absorption path located mainly over the ocean, reflecting the domination of the inter-tidal region as an iodine source at Mace Head, led to further improvement. The results are compared with previous measurements at Mace Head, and elsewhere in the remote

marine boundary layer.

1. Introduction

Hydroxyl radicals (OH) are the principal oxidising species in the troposphere, and dominate the daytime removal of most volatile organic compounds (VOCs) (Levy, 1971; Logan et al., 1981). Reaction with OH thus governs the atmospheric lifetime of many species, and hence their potential to contribute to (for example) climate change and ozone depletion. The OH-initiated oxidation of hydrocarbons and CO in the presence of oxides of nitrogen also leads to the generation of ozone, a constituent of photochemical smog. Improving our understanding of the abundance and distribution of OH is thus a key goal of atmospheric chemistry. As the reactivity of OH is high, its concentration is low (of the order of 0.04–0.2 pptv in the sunlit troposphere) and its chemical lifetime is short (0.1–1 s); OH concentrations are therefore determined by local chemical processes rather than transport. Comparison of in situ measurements of HO_x ($OH+HO_2$) with calculations and box model simulations constrained by observations of longer-lived species such as NO_x ($NO+NO_2$), ozone and VOCs can thus be used to test our understanding of these processes, and to validate the chemical mechanisms included in tropospheric models. This paper describes observations and steady-state analyses of marine boundary layer OH and HO_2 concentrations measured at Mace Head, Ireland.

In the summer of 2002 the Universities of Leeds, York, East Anglia, Leicester, UMIST (now Manchester), Birmingham, Aberystwyth, Bristol, Cambridge, Edinburgh and the National University of Ireland (NUI) Galway participated in the NAMBLEX (North Atlantic Marine Boundary Layer EXperiment) campaign, located at the Mace Head Atmospheric Research Station, near Carna, County Galway on the west coast of Ireland (53°23′ N, 9°54′ W). The Mace Head site has a clean air sector extending from 180 to 300° encompassing the prevailing westerly winds, and the site experiences a range of clean and semi-polluted air masses arriving mainly from the Atlantic but also from the

Arctic, Europe and the United Kingdom (Cape et al., 2000; Simmonds et al., 1996). Further details of the NAMBLEX campaign and the Mace Head site can be found in the NAMBLEX overview paper in this issue (Heard et al., 2005).

Mace Head has been the location for several previous field campaigns at which OH and HO_2 have been measured (Creasey et al., 1997; Creasey et al., 2002; Berresheim et al., 2002) and compared with simulations using constrained numerical box models. In particular, the NAMBLEX project followed on from the EASE96 (East Atlantic Summer Experiment) and EASE97 (Spring) campaigns during which the University of Leeds FAGE (Fluorescence Assay by Gas Expansion) instrument was also deployed for the measurement of OH and HO_2. During EASE96 and 97, OH and HO_2 were observed with midday concentrations of $(2.0–6.0)\times10^6$ and $(0.5–3.5)\times10^8$ molecule cm^{-3}, respectively (Creasey et al., 2002). The OH concentrations correlated well with the OH production rate from ozone photolysis during periods when clean air, originating in the arctic (low NO_x), arrived at Mace Head. Carslaw et al. (2002) used a constrained photochemical box model based upon the Master Chemical Mechanism (MCM http://mcm.leeds.ac.uk/MCM) (Carslaw et al., 1999a; Jenkin et al., 1997) to simulate OH and HO_2 during EASE97. It was found, on average, that the model substantially overpredicted OH and HO_2 by factors of 2.4 and 3.6, respectively, for data obtained between 11:00 and 15:00 GMT. OH was also measured at Mace Head by Chemical Ionisation Mass Spectrometry (CIMS) during the PARFORCE experiment in 1999 (Berresheim et al., 2002). A mean daily maximum OH of $(2.6\pm0.5)\times10^6$ molecule cm^{-3} was observed, but calculations using a simple box model overestimated OH concentrations by an average factor of 8.2.

HO_x measurements at other remote marine boundary layer locations have tended to indicate typical maximum levels of OH of up to $(3.0–6.0)\times10^6$ molecule cm^{-3}, and HO_2 of up to $(1.0–2.5)\times10^8$ molecule cm^{-3} (ca. 4–10 pptv). Agreement between observed OH and calculations using constrained box-models has been reasonably good with model/measurement ratios of 1.15 (Cape Grim, Tasmania – SOAPEX-2 – Sommariva et al., 2004), 1.17 (South Atlantic – ALBATROSS – Brauers et al., 2001) and

0.80 (Christmas Island, Pacific Ocean – PEM Tropics A – Chen et al., 2001). In contrast, for HO_2, models have tended to overestimate the measurements, with reported model/measurement ratios of 1.4 (SOAPEX-2 – Sommariva et al., 2004), 0.8 and 2 (Okinawa and Oki Islands, respectively – ORION-99 – Kanaya et al., 2001a) and 1.7 (Rishiri Island – Kanaya et al., 2002). Given the importance of quantitative prediction of tropospheric HO_x for determination of the atmospheric oxidative capacity, improvements are required in our understanding of the chemistry occurring in (nominally) clean environments such as the remote marine boundary layer.

From the perspective of HO_x chemistry, the NAMBLEX campaign featured several improvements to the data coverage compared with previous studies at Mace Head and elsewhere in the marine boundary layer, notably measurement of a more comprehensive suite of OH sinks, including previously unmeasured oxygenated VOCs (*o*-VOCs) (Lewis et al., 2005), measurement of the HO_2 co-reactants IO and BrO (Saiz-Lopez et al., 2004a, b, 2005a, b), and detailed aerosol chemical composition and size distribution (Coe et al., 2005). The OH and HO_2 measurements were performed simultaneously rather than sequentially, permitting a more accurate constraint of the flux between the HO_x species. In contrast with the EASE96 and EASE97 campaigns, the measurements of radical species (NO_3, OH/HO_2, RO_2) were co-located at the shoreline site, together with the aerosol, VOC, O_3 and meteorological measurements. Previously the instruments had been separated by up to 200 m, leading to concerns that instruments may have sampled different air masses following the formation of an internal boundary layer as the oceanic air encounters the shoreline (Carslaw et al., 2002).

This paper describes the NAMBLEX HO_x measurements and analyses of the OH and HO_2 concentrations using the steady-state approximation. Comparisons of the measurements with the predictions of a constrained box model are described in a separate paper (Sommariva et al., 2005). The paper is structured as follows: The basic HO_x photochemical relationships are given in Sect. 2, followed by a description of the experimental technique, including the calibration, precision and accuracy of the FAGE system, in Sect. 3. The OH and HO_2 dataset is described in Sect. 4, including a discus-

sion of four representative "case study" days. In Sect. 5, the relationship between OH and the rate of ozone photolysis ($j-(O^1D)$) is considered (5.1), followed by an examination of the ability of steady state expressions of increasing complexity to simulate the measured OH (5.2) and HO_2 (5.3) concentrations. Finally, in Sect. 6, the results from NAMBLEX are discussed and placed in the context of related analyses undertaken for similar environments.

2. Tropospheric HO_x photochemistry

The major OH production pathway in the troposphere is photolysis of ozone at wavelength of light ≤340 nm, followed by reaction of the resulting electronically excited O^1D atoms with water vapour, in competition with their collisional quenching. This primary production rate for OH, P(OH), is given by:

$$P(OH)=2f[O_3]j-(O^1D) \tag{1}$$

where $j-(O^1D)$ is the rate of O_3 photolysis by sunlight to generate O^1D and f is the fraction of O^1D that reacts with water vapour to produce OH, rather than undergoing collisional quenching with N_2, O_2 or H_2O to form O^3P:

$$f = \frac{k_{O^1D+H_2O}[H_2O]}{k_{O^1D+H_2O}[H_2O] + k_{O^1D+N_2}[N_2] + k_{O^1D+O_2}[O_2]} \tag{2}$$

Under normal mid-latitude marine boundary layer conditions f takes values of around 0.1–0.2 (minor quenching species, such as CO_2, are neglected).

The major sinks for OH under clean conditions are CO, CH_4 and VOCs, resulting in production of HO_2 and other peroxy radicals (RO_2). HO_2 is also produced through reaction of OH with O_3 and photolysis of HCHO, and is recycled to OH through reaction with O_3 and NO. HO_x chain termination occurs via radical recombination reactions (HO_2+HO_2, HO_2+RO_2 and $OH+HO_2$) and by the reaction of OH with NO_2, the former

dominating in clean air, the latter in polluted air. The lifetime of OH is typically less than 1 s and consequently OH rapidly reaches photochemical steady state, given by:

$$[OH]_{ss} = \frac{\text{rate of production}}{\sum_i k_{OH+i}[i]} \quad (3)$$

where each i represents an OH co-reactant. If O_3 photolysis is the only OH production mechanism, and reaction with CO and CH_4 are the only sinks, $[OH]_{ss}$ is given by:

$$[OH]_{ss} = \frac{P(OH)}{k_{OH+CO}[CO] + k_{OH+CH_4}[CH_4]} \quad (4)$$

Equation (4) can be extended to incorporate additional OH sources (e.g., HO_2+NO) and sinks (e.g., reaction of OH with H_2, NO_2 and dimethylsulphide, DMS). Section 5 of this paper assesses how comprehensive a selection of OH precursors and co-reactants is required to satisfactorily simulate measured OH concentrations at Mace Head.

Steady-state calculations of HO_2 are more complicated than those of OH, as they must take into account both the fast interconversion with OH, and the second order HO_2 removal processes, HO_2+HO_2 and HO_2+RO_2. Expressions deriving a relationship between HO_2 and the square root of $j-(O^1D)$ have been used previously (e.g., Penkett et al., 1997), but require assumptions regarding the HO_2:RO_2 ratio and neglect certain HO_2 removal terms. In this work, we have adopted the cubic equation for HO_2 developed by Carslaw et al. (1999b, 2002):

$$\beta[HO_2]^3 + \gamma[HO_2]^2 + \delta[HO_2] + \varepsilon = 0 \quad (5)$$

where β, γ, δ, and ε are derived from a reduced "mini" mechanism of the MCM (25 reactions and 17 species), and contain measured concentrations of long-lived species, together with radiative and kinetic parameters (see Appendix A). The "mini" mechanism was shown to be valid under clean conditions at Mace Head, with HO_2 concentrations calculated from the solution of expression (5) being within 20% of calculations carried out using the full, near-explicit MCM, containing ca. 1500 reactions (Carslaw et al., 1999b, 2002).

3. Experimental

OH and HO_2 radicals were measured using laser-induced fluorescence (LIF), via the FAGE (Fluorescence Assay with Gas Expansion) technique (Hard et al., 1984; Heard and Pilling, 2003). The instrument used was an improvement of that deployed in previous campaigns (e.g., Creasey et al., 2003), with several significant modifications (described below), notably the use of two detection channels enabling simultaneous (rather than sequential) measurement of OH and HO_2, implementation of an all solid state laser system, and use of a fibre-optic system for delivery of the UV radiation to the fluorescence cells. The instrument was housed in an air-conditioned 20 foot shipping container, fitted out as a mobile laboratory. The laser system, fibre launch optics, photon counting electronics, computer and pumping system were located inside the container whereas the fluorescence cells, detectors and gating electronics were housed in a weatherproof box on the container roof.

The FAGE system was located at the "shoreline" measurement site at Mace Head, approximately 50 m horizontally and 10 m vertically (inlet height) from the high-water mark. A plan of the Mace Head site is shown in the NAMBLEX overview paper in this issue (Heard et al., 2005), indicating the relative positions of the various instruments. The fetch from the shoreline was unobstructed by buildings or other instruments. The container was mounted on a flatbed trailer, giving a sampling height ca. 5 m above ground level. A schematic diagram of the overall layout of the instrument is shown in Fig. 1.

3.1. Instrumental details

The FAGE technique uses 308 nm on-resonance laser-induced fluorescence to detect OH radicals, employing a low-pressure gas expansion to extend the fluorescence lifetime and permit temporal discrimination between scattered laser light and OH fluorescence. The gas expansion also ensures rapid refreshing of the gas in the fluorescence region, enabling use of a high pulse repetition frequency, low pulse energy excitation

laser which minimises any photolytically induced interferences while giving the sensitivity necessary to detect OH at ambient levels. In the Leeds system, ambient air is expanded into two low-pressure fluorescence cells, one of which is used for OH detection, and the other (through addition of NO, and hence conversion of ambient HO_2 to OH) for the detection of HO_2.

During NAMBLEX, a novel all solid-state, Nd:YAG pumped Ti:Sapphire laser was used to generate 308 nm radiation used for OH excitation, in place of the copper vapour pumped dye laser used previously. A full description of the laser system is given in Bloss et al. (2003); illustrative details will be given here. The pump laser is a diode-pumped, intra cavity doubled, Q-switched, Nd:YAG laser (Photonics Industries DS 20-532), which produces ~10 W of 532 nm radiation at a repetition frequency of 5 kHz. The 532 nm radiation is used to pump a water cooled Ti:Sapphire crystal, producing broadband near IR radiation in the range 690–1000 nm. The Ti:Sapphire oscillator wavelength of approximately 924 nm is selected using a diffraction grating, with computer control of the grating angle. The fundamental wavelength from the Ti:Sapphire is then passed through two non-linear harmonic generation stages consisting of two cerium lithium borate crystals, producing 462 nm and 308 nm radiation by second and third harmonic generation, respectively. The beam profile produced by the laser cavity design contains a number of longitudinal modes such that following harmonic generation, a spectral linewidth of ~0.065 cm^{-1} is produced, thus providing efficient overlap with the Doppler broadened OH spectral profile at 308 nm under the low pressure conditions of the FAGE instrument (approximately 0.08 cm^{-1}). The $Q_1(2)$ branch of the OH $A^2\Sigma^+$ (v'=0) – $X^2\Pi_i$ (v''=0) transition was excited at 307.999 nm. Approximate (±0.002 nm) wavelength tuning is provided by splitting a small fraction of the second harmonic radiation into a wavemeter. Precise tuning to the peak of the spectral line of OH is then achieved by use of a reference fluorescence cell containing a high [OH] (produced by a microwave discharge of water vapour in ambient air at 5 Torr). Upon exiting the laser, the UV radiation is passed through a series of dielectric beamsplitters and split into three fractions of 5%, 25% and 70% power. The 5% fraction of the

radiation is directed into the reference cell for wavelength calibration. The 70% and 25% fractions are focussed into fibre optic cables (length=5 m) for transmission of the light into the OH and HO_2 measurement cells, respectively, positioned on the roof of the container. Upon exiting the fibres, the light is collimated using a plano-convex lens, and passed through the detection cells via baffled side arms, providing a 10 mm diameter laser beam in the excitation region. The total light transmission through the fibre optic system from the beamsplitter to the centre of the detection cell was ~60%. After traversing each cell, the laser beam exits via a second baffled side-arm and is directed onto a UV sensitive photodiode, enabling the laser power in each cell to be monitored continuously for subsequent normalisation of the OH LIF signal for any fluctuations in laser power. Typically, the laser power entering the OH and HO_2 detection chambers was ~20 mW and ~5 mW, respectively.

The detection cells comprised 220 mm internal diameter cylindrical chambers, with internal surfaces sand blasted to minimise reflections. Each cell pressure was monitored by a capacitance manometer, and was independently adjustable through butterfly valves located at the cell exit prior to the roots/rotary pumping system. The nozzle arrangement differed for OH and HO_2 to maximise OH sensitivity and HO_2 conversion efficiency, respectively. For the OH cell, ambient air was expanded through a 0.8 mm flat nozzle, with a flow rate of ca. 4.8 slm, into the fluorescence chamber held at a pressure of 0.9 Torr. The gas expansion intersected the laser and detection axes approximately 90 mm below the nozzle. The HO_2 cell had a reduced nozzle diameter of 0.6 mm (total flow rate into the cell was ca. 3.6 slm), an increased nozzle to laser-axis distance of 400 mm, and featured an NO injection ring positioned concentrically around the gas beam, ~250 mm below the nozzle. The injection of NO well downstream of the initial gas expansion (containing the supersonic region) resulted in better mixing of the NO with the gas stream, compared with injection directly beneath the nozzle. NO was injected with a flow of 140 sccm into the beam, resulting in conversion of approximately 75% of the ambient HO_2 to OH. The OH and HO_2 cell inlets were separated horizontally by approximately 70 cm. The LIF signal from the HO_2 channel arises from OH

converted from ambient HO_2 plus ambient OH.

The fluorescence collection axes, perpendicular to the laser beam, comprise collimating lenses, a narrow bandwidth interference filter (transmission >50% at 308 nm, FWHM=8.0 nm) and focussing lenses to direct the 308 nm radiation onto the 8 mm diameter photocathode of a channeltron photomultiplier (CPM). The solid angle of fluorescence collected was approximately doubled using a spherical mirror mounted opposite the collection optics. The CPM was switched off ~2 μs before the laser pulse using a gating system developed at Leeds (Creasey et al., 1998) to provide a +100 V potential difference on the cathode relative to the channeltron body. The CPM is held in this low gain state until ~100 ns after the peak of the laser pulse. The CPM is then switched back to the high gain state in order to collect the OH fluorescence signal. The CPM signal is amplified and recorded using photon counting techniques, during a 500 ns wide integration window, commencing 100 ns after the peak of the laser pulse. A second integration window, delayed 50 μs after the laser pulse with a width of 5 μs, was used to measure the signal from solar scattered light entering the chamber through the nozzle, for subsequent subtraction.

The computer controlled data acquisition sequence in the OH cell is as follows: (1) The centre of the $Q_1(2)$ line is located by scanning the laser wavelength across a 0.005 nm region encompassing the peak of the line whilst recording the reference cell signal, and then adjusting the wavelength to the line peak (such that the reference cell signal reached at least 90% of its maximum). (2) The wavelength is then kept constant for a period of 200 s (consisting of 10 points, where 1 data point is acquired every 20 s), during which the sum of laser scatter and OH fluorescence signal (with the contribution from solar scatter subtracted) is recorded. (3) The wavelength is then stepped down by 0.005 nm, so that the laser is no longer on-resonance with the OH spectral line, allowing the signal solely due to laser scattered light to be collected for subsequent subtraction. This background signal is collected for 100 s (5 points of 20 s averaging). (4) The OH fluorescence signal is then normalised to laser power using the signal from the UV photodiode situated after the exit arm of the cell. For the HO_2 cell, the data

acquisition sequence is the same as for the OH cell, but NO is added to the chamber. The flow of NO is switched off part way through the background points (laser not on resonance with OH) to check for any increased background due to the presence of NO (which was not observed). A small (<5%) correction was required as the "HO_2" cell signal contains a contribution due to ambient OH; this was subtracted using the OH concentration determined in the other cell, adjusted for the relative OH sensitivities between the cells.

3.2. Calibration

[OH] sampled at the nozzle is directly related to the observed signal, S, by a calibration constant, C_{OH}, and the laser power, P:

$$S = C_{OH} P [OH] \tag{6}$$

C_{OH} cannot be calculated accurately as it depends on parameters that are hard to measure such as the optical collection and sampling efficiency. C_{OH} was therefore determined empirically using the H_2O photolysis/O_3 actinometry method (Schultz et al., 1995). Briefly, synthetic air with a known concentration of H_2O (determined by an infra-red absorption spectrometer with a precision and accuracy of 0.02% v/v, and a response time of 5 s), was flowed at 12 slm through a quartz flow tube (0.6 m long, 22 mm internal diameter) held vertically above the inlet nozzle. The air was exposed to 184.9 nm radiation from a mercury pen-ray lamp with an axial irradiation zone of length 23 mm. The centre of the irradiation zone is 64 mm above the inlet nozzle, with a transit time to the nozzle of ca. 0.1 s. Photolysis of water vapour at 184.9 nm leads to the production of OH radicals and H atoms. HO_2 radicals are rapidly formed by the reaction of H atoms with ambient O_2. The OH and HO_2 production was quantified relative to the concomitant formation of O_3 following the photolysis of O_2 :

$$H_2O + h\nu \rightarrow OH + H \tag{R1}$$

$$H + O_2 + M \rightarrow HO_2 + M \tag{R2}$$

$$O_2 + h\nu \rightarrow 2O \quad \text{(R3)}$$

$$2(O + O_2 + M \rightarrow O_3 + M) \quad \text{(R4)}$$

Approximately 4.8 slm of the calibration gas was sampled through the inlet nozzle (3.6 slm in the case of the HO_2 cell), with the remaining gas forming an excess flow, in which O_3 was measured using a UV photometric detector (precision and accuracy of ±0.6 ppbv and detection limit of 0.4 ppb for 1 min averaging), enabling [OH] and [HO_2] to be calculated through knowledge of the relevant quantum yields and cross sections:

$$[OH] = [HO_2] = \frac{[O_3][H_2O]\sigma_{184.9\,nm(H_2O)}\phi_{HO_x}}{[O_2]\sigma_{184.9\,nm(O_2)}\phi_{O_3}} \quad (7)$$

where $\phi_{OH}=\phi_{HO_2}=1$ and $\phi_{O_3}=2$ are the quantum yields for production of OH, HO_2 and O_3, respectively. The ozone concentration used to calculate the OH level at the inlet nozzle, via Eq. (7), was corrected by a profile factor, which accounts for the variation in axial velocity across the laminar flow in the calibration tube, defined as $[O_3]_{excess}/[O_3]_{centre}$, which was determined experimentally to be 1.94±0.07. Several studies have shown that the effective absorption cross section of O_2 at 185 nm depends on the individual photolysis lamp used (and its operating conditions) and the O_2 column through which the radiation propagates (Cantrell et al., 1997; Creasey et al., 2000; Hofzumahaus et al., 1997) and as a result $\sigma_{184.9\,nm(O_2)}$ was measured for the actual lamp and operating conditions used in the field calibrations.

OH and HO_2 calibrations were carried out daily during the NAMBLEX campaign. The calibration constants for both the OH and HO_2 cells were insensitive to changes in water vapour under the (moist) conditions typically experienced at Mace Head (H_2O=0.5–2.2%). As a result, the daily calibrations were carried out using a H_2O mixing ratio of ca. 0.7% and O_3~2.5 ppbv, resulting in [OH] and [HO_2] levels of the order of 10^9 molecule cm^{-3}. In separate tests, multipoint calibrations, involving attenuation and measurement of the relative 184.9 nm flux, and carried out at constant [H_2O], have demonstrated that the instrument has a linear response to [OH] and [HO_2] in the range

10^7–10^9 molecule cm^{-3}, and thus the daily calibration was applicable to atmospheric levels of [OH] and [HO_2]. During NAMBLEX, the mean OH calibration constant C_{OH} was (1.76±0.38)×10^{-7} cts molecule^{-1} cm^3 s^{-1} mW^{-1}. The analogous HO_2 calibration constant C_{HO_2} was (3.28±1.21)×10^{-8} cts molecule^{-1} cm^3 s^{-1} mW^{-1} during the campaign (where the mean C_{OH} for the HO_2 cell was (4.30±0.84)×10^{-8} cts molecule^{-1} cm^3 s^{-1} mW^{-1}). The difference arises as a consequence of the incomplete conversion of HO_2 to OH, and the differences in expansion jet geometry between the cells. C_{HO_2} was determined either by converting the OH in the calibration flow-tube to HO_2 via the addition of CO, or by measuring the additional OH LIF signal when NO was added to the HO_2 cell, giving very similar results.

Assuming Poisson statistics, the lower detection limit for OH is given by (Stevens et al., 1994):

$$[\mathrm{OH}]_{\mathrm{min}} = \frac{S/N}{CP}\sqrt{\left(\frac{1}{m}+\frac{1}{n}\right)}\sigma_b \tag{8}$$

$$\sigma_b = \sqrt{\frac{1}{t}\left(S_{lb}+S_{sb}+S_{db}\right)} \tag{9}$$

where S/N is the signal-to-noise ratio, P (mW) is the laser power, m is the number of data points of OH signal, n is the number of background data points, t (s) is the averaging time for each data point, and S_{lb}, S_{sb}, S_{db} (cts s^{-1}) are the background signals due to laser scatter, solar scatter and the PMT dark count, respectively. The detection limit was calculated for each day on which measurements were made using Eqs. (7) and (8) with S/N=1, t=20 s, S_{db}=0, m=10, n=5, actual S_{lb} and S_{sb} from around solar noon, and C_{OH} from the most recent calibration. These daily detection limits were then averaged to give the mean daytime lower detection limit for [OH] of (1.91±0.64)×10^5 molecule cm^{-3} over a 300 s data collection period. At night, the detection limit improved as S_{db}=0 and so the mean night-time lower detection limit for

[OH] was found to be $(6.09\pm2.75)\times10^4$ molecule cm^{-3}. The corresponding mean values for $[HO_2]$ were found to be $(2.94\pm1.05)\times10^6$ molecule cm^{-3} (0.11 pptv) during the day and $(1.02\pm0.39)\times10^6$ molecule cm^{-3} (0.04 pptv) at night. The accuracy in the reported measurements is determined by the calibration factors and is 22% and 25%, respectively, (1σ) for OH and HO_2. The precision of the instrument (quoted as a percentage) depends upon the signal magnitude (i.e. upon the concentration measured), and is determined by fluctuations in the background signal (solar and laser-induced). The standard deviation of the background signal was 2.6 counts s^{-1}, and hence for $[OH]=3\times10^6$ molecule cm^{-3}, the precision is 20%, giving a total uncertainty in quadrature of 30%. For $[HO_2]=1\times10^8$ molecule cm^{-3} (4 pptv), the corresponding 1σ uncertainty is 28%.

4. Results

4.1. Overview of the HO_x data set

During the NAMBLEX campaign OH measurements were made on 24 days between 25 July and 1 September 2002, whilst due to technical difficulties HO_2 was only measured on 17 days, between 31 July and 1 September. Figure 2 shows the time series of OH and HO_2 for the entire campaign. Each measurement is an average of 10 adjacent 20 s data points within a 5 min data collection cycle (taking into account the background period of 5 adjacent 20 s data points). The corresponding values of $j-(O^1D)$ averaged over 5 min are also shown. OH has a clearly defined diurnal profile with absolute daytime maxima around local solar noon (12:45 GMT at Mace Head) varying between $(3–8)\times10^6$ molecule cm^{-3}. Figure 3a shows the average diurnal profile of OH over the entire measurement period. The 24 h mean OH concentration (derived from hourly means) was found to be 9.1×10^5 molecule cm^{-3}. A diurnal pattern is again exhibited for HO_2, although on some days it is less pronounced (for example, Fig. 2, 21 August). Daytime maxima varied between $0.9–2.1\times10^8$ molecule cm^{-3} (~3.5–8.2 pptv). Data

taken on the night of 31 August–1 September (Fig. 2) provides significant evidence to support the presence of night-time HO_2 radicals, with observed concentrations of (2–3)×10^7 molecule cm^{-3} (0.8–1.2 pptv) (c.f. mean HO_2 night-time detection limit of 1.8×10^6 molecule cm^{-3} (0.04 pptv)) as observed previously at Mace Head (Creasey et al., 2002; Salisbury et al., 2001). Figure 3b shows the average diurnal profile of HO_2. The 24 h mean HO_2 concentration was found to be 4.2×10^7 molecule cm^{-3} (1.7 pptv). Both the OH and HO_2 24 h mean concentrations include relatively few night-time observations, however their abundance is expected to be dominated by daytime values. Analysis of the dependence of the ratio of [HO_2]/[OH] on NO was carried out using three NO bins of 0–10, 10–30 and 30–500 pptv for which the ratio [HO_2]/[OH] was found to be 119, 73 and 53, respectively. This behaviour is quantitatively similar to that seen during the EASE97 field campaign which took place at Mace Head when the [HO_2]/[OH] ratio was seen to reduce from 80 to 34 as the average NO level increased from 42 to 279 pptv (Creasey et al., 2002). The data from the campaigns clearly illustrates how the ratio [HO_2]/[OH] falls as NO increases due to the increased rate of recycling of HO_2 to OH.

4.2. Case studies

In this subsection a detailed description is given of the chemical and meteorological conditions for several days during the NAMBLEX campaign which will provide the focus for further analysis in Sect. 5. Time series for OH, HO_2, j–(O^1D), NO, NO_2, wind direction, O_3 and H_2O vapour, together with daily averages of CO, CH_4 and three *o*-VOCs (methanol, acetaldehyde and acetone), for 15, 16, 18 and 21 August are shown in Fig. 4. Days were chosen when considerable periods of both OH and HO_2 data were available. There are many other days containing long time series of OH data, and these are considered in further detail in Sommariva et al. (2005a).

4.2.1. 15 August – Figure 4a

15 August has a relatively smooth diurnal profile for $j-(O^1D)$. Prevailing winds were from a South Westerly direction throughout the day and the trajectory air mass classification for this day was found to be South Westerly (Heard et al., 2005; Norton et al., 2005). The example back trajectory for a South Westerly air mass classification (see Fig. 20d in Heard et al., 2005) illustrates that the air had not recently passed over land resulting in clean air with daily average NO and NO_2 mixing ratios of 6.2 and 25.9 pptv, respectively. Suppression of $j-(O^1D)$, [OH] and [HO_2] occurred around 12:00 and 13:40 GMT when several large clouds passed over the site. A short lived spike in [HO_2] of 1.4×10^8 molecule cm^{-3} at 16:51 GMT was accompanied by a rapid reduction in [OH] to 1.9×10^5 molecule cm^{-3}, although there were no concurrent spikes in O_3, CO or H_2. However, it must be noted that the latter two species were measured with 45 min averaging times and so it is difficult to observe rapid changes. Thorough inspection of signals and other diagnostic data from both the OH and HO_2 cells finds that there were no instrumental deficiencies causing this short lived (50 s) peak in [HO_2]. Three moderate spikes in both NO (between 33 and 90 pptv) and NO_2 (between 90 and 201 pptv) were observed between 06:00 and 18:00 GMT. [OH] reached a peak daytime value of 3.3×10^6 molecule cm^{-3} at 12:28 GMT whilst at the same time [HO_2] dropped to 8.9×10^7 molecule cm^{-3} (occurring slightly before a dip in $j-(O^1D)$), perhaps the result of a small peak in NO (28.4 pptv) increasing the rate of recycling of HO_2 to OH.

4.2.2. 16 August – Figure 4b

The meteorological conditions experienced on 16 August were less stable than those experienced on 15 August with wind direction changing from South Westerly to South Easterly throughout the course of the day. Measurements of both OH and HO_2 began at 06:45 GMT with concentrations of 7.5×10^5 and 3.6×10^7 molecule cm^{-3}, respectively, which continued to rise steadily until 10:33 GMT when both [OH] and [HO_2]

dropped due to a reduction in $j-(O^1D)$. This was then followed by a peak in [OH] of up to 4.5×10^6 molecule cm^{-3}, whereas $[HO_2]$ continued to fall due to the steady rise in the levels of NO to 125 pptv causing an increase in the rate of recycling of HO_2 to OH. Following this [OH] dropped suddenly to 7.3×10^5 molecule cm^{-3} at the same time as a peak in NO_2 (>950 pptv) and drop in $j-(O^1D)$. Levels of HO_2 also fell to 2.5×10^6 molecule cm^{-3} due to a continued rise in NO (458 pptv). Although there are gaps in the NO and NO_2 data it is clear to see that there was a second peak in both species just after 12:00 GMT accompanied again by a drop in [OH] and another dramatic drop in $[HO_2]$ from which both species recover by ~12:40 GMT when levels of NO and NO_2 reduced (to ~35 and 120 pptv, respectively). Levels of both OH and HO_2 begin to fall together with $j-(O^1D)$ from 13:50 GMT onwards. There are several bursts of [OH] throughout the afternoon and early evening which are correlated with relatively short lived peaks in NO. $[HO_2]$ levelled off to an average of 3.5×10^7 molecule cm^{-3} from 16:08 GMT onwards whilst [OH] continued to fall to below the detection limit until 18:55 GMT. After this time a peak in NO appears to coincide with a revival in [OH] to close to the detection limit (average [OH] from 18:55 to 20:23 GMT=2.1×10^5 molecule cm^{-3}) where it persisted until measurements stopped at 20:23 GMT.

4.2.3. 18 August – Figure 4c

The air mass classification for 18 August shows Cyclonic conditions where the wind was coming from a South Westerly direction at the beginning of the day and swings round to the North West from ~06:00 GMT onwards (Heard et al., 2005). NO and NO_2 remain fairly constant throughout the majority of the daylight hours. NO_2 was elevated for several hours around 06:00 GMT and from 18:00 GMT onwards whilst at the same time there was some depression in NO. There was also a relatively short lived spike in NO_2 (~15 min) of up to 350 pptv at ~07:55 GMT. Measurements of [OH] and $[HO_2]$ began at 08:27 GMT with levels rising together with $j-(O^1D)$. Daytime maxima in both [OH] and $[HO_2]$ of 3.3×10^6 and 1.1×10^8 molecule cm^{-3} were reached at 13:47 GMT,

rather late as there was a cloudy period around solar noon with reduced $j-(O^1D)$. Both [OH] and $[HO_2]$ then decrease with $j-(O^1D)$ until 17:12 GMT when both species remain fairly constant whereas $j-(O^1D)$ continues to decrease. This observation may be indicative of alternative photolytic sources or reduced levels of sinks, and was replicated on several days of the campaign. Measurements stopped at 20:39 GMT by which time [OH] had fallen to close to the detection limit. $[HO_2]$ remained relatively constant between 18:29 and 20:01 GMT with an average of 1.2×10^7 molecule cm^{-3} and then increased by a factor of 2 in the 38 min before measurements stopped. There is also some evidence at the same time for a small peak in the concentration of total peroxy radicals $[HO_2]+\Sigma[RO_2]$, as measured by the PERCA instrument (Fleming et al., 2005). Concentrations of IO were significant around midday (up to 5 pptv).

4.2.4. 21 August – Figure 4d

The air mass classification for 21 August is a mixture of Cyclonic and South Westerly (Heard et al., 2005), with a change of wind direction from South Easterly to South Westerly throughout the course of the day. The chemical conditions are unsettled with several relatively large and long lived peaks in NO and NO_2, beginning early in the morning and persisting until midday. This variability in NO_x resulted in considerable structure in the diurnal behaviour of [OH] and $[HO_2]$ in addition to that expected due to the changes in $j-(O^1D)$. There were two intervals starting at 06:54 and 08:06 GMT when [OH] flattened off rather than continuing to rise with $j-(O^1D)$ which appear to be linked to spikes in NO_2 of 0.37 and 1.3 ppbv. The peak in $[OH]=8.08\times10^6$ molecule cm^{-3} on this day was one of the highest observed during the campaign, and occurred at 09:50 GMT well before solar noon, when levels of NO_2 were quite low (400 pptv). OH levels show further rises and falls correlated with the structure in NO_2 until the afternoon when NO_x levels become very low. OH levels fall to very low values ($\sim5\times10^5$ molecule cm^{-3}) around 15:00 GMT which persist for a considerable period followed by a secondary peak (up to 4.4×10^6 molecule cm^{-3}), that coincides with a secondary maximum in

$j-(O^1D)$ and very low NO_2 levels. The $[HO_2]$ diurnal profile has considerable structure correlated with changes in NO, for example the large dips in HO_2 at ~09:03 and 10:30 GMT coincide with NO spikes of 490 and 1222 pptv, respectively. $[HO_2]$ and $j-(O^1D)$ reached their daytime maximum around 13:00 GMT, ~3 h later than for OH. In the afternoon $[HO_2]$ then fell steadily with $j-(O^1D)$ before increasing slightly and levelling off to an average concentration of 1.3×10^7 molecule cm^{-3} towards the end of the measurements (which ended at 19:56 GMT).

5. Data analysis and interpretation

5.1. $j-(O^1D)$ dependence of OH

The dependence of OH upon the rate of production of electronically excited oxygen atoms, $j-(O^1D)$, depends upon the chemistry dominating OH production. In the absence of NO_x, primary production via O_3 photolysis and the subsequent O^1D+H_2O reaction is expected to dominate, and OH should show an approximately linear relationship with $j-(O^1D)$, with some deviation due to HO_2+O_3. At higher NO levels, the HO_2+NO reaction and HONO photolysis are of increasing importance as sources of OH and the relationship between OH and $j-(O^1D)$ becomes more complex.

In their analysis of OH data acquired at a rural site in Germany, Ehhalt and Rohrer (2000) have shown that for a particular NO_x level the dependence of OH upon $j-(O^1D)$ can be better described by an expression of the form $OH=a\times j-(O^1D)^b$, where the non-unity exponential parameter b incorporates the influences of for example, $j-(NO_2)$ and $j-(HONO)$ upon OH production, via HO_2+NO and HONO photolysis, respectively. This analysis was subsequently applied by Berresheim et al. (2003) to OH data acquired during the MINOS campaign on the North Eastern coast of Crete in 2001, where a=1.39–2.2 and b=0.68, was found to describe their data well.

At Mace Head, radical production from NO_3 initiated hydrocarbon oxidation and

alkene ozonolysis has been observed previously (Salisbury et al., 2001), consequently we have examined the use of a modification to the expression used by Berresheim et al. (2003) to include an intercept, which can account for non-photolytic OH production:

$$[\mathrm{OH}]/10^6\,\mathrm{molecule\,cm^{-3}} = a \times \left(j - (\mathrm{O^1D})/10^{-5}\,\mathrm{s^{-1}}\right)^b + c \qquad (10)$$

Inclusion of the intercept should allow a better description of the data during twilight and overnight; also determination of the parameters a, b and c from predominantly daytime OH and j–(O^1D) data could constrain the levels of OH anticipated overnight, if the nighttime production mechanisms continue during daylight hours – as expected for alkene ozonolysis but not NO_3. The coefficients in Eq. (10) were optimised by least-squares fitting to the observed OH concentrations and j–(O^1D) values, the latter measured by a 2-π spectral radiometer (see Heard et al., 2005, this issue, for further details). Fits were performed for a linear form of Eq. (10) (b=1, c=0) (1), a simple power function (c=0) (2), or a power function with an intercept (3), as shown in Table 1. The experimental scatter plot of [OH] versus j–(O^1D) and associated fits with Eq. (10) are shown in Fig. 5. While the improvement in correlation coefficient (r^2) between the successive fits is modest (partly reflecting the high scatter of the data when all plotted together), visual inspection of the scatter plot shows that fits (2) and (3) clearly better describe the data than the simple linear fit (1).

The dependence of OH upon j–(O^1D) is itself dependent upon NO_x, as noted by Ehhalt and Rohrer (2000). During NAMBLEX, the envelope of NO_x (ca. 5–2000 pptv) encompassed the range from "clean" to "polluted" conditions, such that single values for a, b and c are not necessarily applicable to the entire dataset. We have therefore repeated the fitting analysis, with the data in three NO bins, covering 0–10, 10–30 and 30–500 pptv (the latter bin approximately equivalent to the conditions during MINOS). The resulting optimised parameters are given in Table 2.

In all cases addition of the power-dependence upon j–(O^1D) results in a better fit than the simple linear expression, with the improvement most marked in the 30–500 ppt NO bin, which corresponds to "intermediate" NO_x conditions, with recycling of HO_2

to OH mediated by the HO_2+NO reaction, and deviation from a simple OH/j–(O^1D) correlation is expected. In general the exponent b is less than 1, corresponding to a "concave" fit to the data, and reflecting the fact that OH rises more rapidly than j–(O^1D) (on average) at low j–(O^1D), possibly due to contributions to HO_x from photolysis of reservoir species such as HONO and/or HCHO, which will have relatively higher photolysis rates at high solar zenith angles (SZA) than for ozone.

In comparison with the results of Berresheim et al. (2003) during the MINOS campaign (a marine environment on Crete), we find the value of b to be lower for the 30–500 pptv NO bin which is most comparable to the MINOS conditions (during which NO_2 ranged from 60–1040 pptv): NAMBLEX, b=0.56±0.03; MINOS, b=0.68±0.01, but the value of a to be slightly higher (NAMBLEX, a=2.29±0.04; MINOS, a=1.39, 1.71 and 2.20 for different time periods). The difference in values of b suggests that non-primary production of OH was more important for Mace Head during NAMBLEX than for Crete during MINOS (also reflected in the much higher scatter apparent in Fig. 5, compared with the equivalent plot for the MINOS dataset). The parameter a relates the steady-state OH level to the solar intensity; during NAMBLEX, typical ozone levels were less than MINOS (approximately 30 vs. 60 ppbv) while the conversion of O^1D to OH was roughly equivalent, thus observation of a comparable value for a may suggest that the OH reactivity (the rate at which it is removed by sinks) was rather higher in the Mediterranean environment of MINOS than in the North Eastern Atlantic environment of NAMBLEX.

Interestingly, addition of the third, intercept parameter c results in little or no improvement to the fits, suggesting that non-photolytic radical production was relatively unimportant over this time period at Mace Head. In the case of the low NO bins, 0–10 and 10–30 pptv, addition of this third parameter results in a reverse of the curvature of the fit (b>1). It is likely that the intercept c (equivalent to 5–6×10^5 molecule cm^{-3}) is higher than the true value of [OH] at night for these conditions, which during NAMBLEX, was measured below 6.09×10^4 molecule cm^{-3}. Hence the parameter b is too high, being a mathematical consequence of the contributions to radical production at

low $j-(O^1D$ from species which undergo photolysis at longer wavelengths than for O^1D production from ozone. This unphysical situation appears to preclude the use of Eq. (10) to estimate nighttime OH levels from predominantly daytime OH data; rather, direct measurement at night is required.

An alternative to the empirical relationship between [OH] and $j-(O^1D)$ is to consider the relationship between [OH] and the rate of primary production of OH, P(OH) (defined in Eq. (1)) during the campaign. If the formation of OH is dominated by ozone photolysis, and the OH removal rate is constant, reflecting constant chemical composition (usually with low NO_x and VOC levels, where OH removal is dominated by reaction with CO and CH_4), a linear relationship between OH and P(OH) is expected (Eq. (4)). Use of P(OH) rather than simply $j-(O^1D)$ incorporates variability in the primary production rate of OH due to changing ozone and water concentrations, and also temperature/pressure. Analysis of [OH] versus P(OH) for 22 days during the NAMBLEX campaign resulted in correlation coefficients (r^2) ranging from 0.13 (21 August, daily average NO=108.4 pptv) to 0.85 (9 August, daily average NO=18.0 pptv), with an average of 0.57 (campaign average NO=31.8 pptv).

5.2. Steady state calculations of [OH]

5.2.1. Assuming production from ozone photolysis and loss by reaction with CO and CH_4 only

In the simplest case, considering only primary production ($O_3+h\nu \rightarrow O(^1D)+H_2O$) and loss through reaction with CO and CH_4, OH concentrations are given by Eq. (4), as outlined in Sect. 2. OH observations were compared with steady-state OH concentrations calculated from Eq. (4) for 200 s data averaging periods from 17 days of the campaign, the period limited by the co-availability of OH, CO and CH_4 data (Heard et al., 2005). The number of days on which steady state OH calculations were possible was increased to 21 by inferring CO and CH_4 levels from their cor-

relations with acetylene and propane measurements (obtained by GC-FID; Lewis et al., 2005), as a strong correlation was observed between these species throughout the campaign (Heard et al., 2005). The CO/acetylene relationship was determined to be (CO/ppbv)=0.27(C_2H_2/pptv)+68.88 (r^2=0.84), from the period 20 h prior to and 22 h subsequent to the gap in the CO data which ran from 04:28 GMT 17 August to 12:40 GMT 21 August. The same method was applied to calculate CH_4 from propane data for the interval from 04:27 GMT 17 August to 09:09 GMT 19 August, using the relationship (CH_4/ppbv)=0.85(C_3H_8/pptv)+1754 (r^2=0.58).

Figure 6 compares the observed OH concentrations with the steady-state values calculated via Eq. (4), for two representative 48 h periods of the campaign. Figure 7 shows the hourly average calculated/observed OH ratio for 8 days (10, 15–21 August) which are used to compare [OH] calculations throughout Sect. 5.2 due to the co-availability of data for calculations using Eq. (12) (Sect. 5.2.2). Figure 7 displays a distinct diurnal profile in which OH is under-predicted early in the morning and in the late afternoon/early evening (high SZA) and over-predicted in the middle of the day. An example of the early morning/late afternoon under-prediction of OH can be seen on 16 August (shown in Fig. 6a), when the calculated/observed OH ratio is less than 1 at the beginning and end of the diurnal. It is unlikely that over-prediction of OH sinks gives rise to the underprediction at high SZA, as Eq. (4) only includes loss of OH by reaction with CO and CH_4. Rather, this behaviour indicates the presence of additional OH sources at these times that are missing in the simple expression, for example recycling of HO_2 through reaction with O_3 and NO, and photolysis of HONO. OH may also be formed through the reaction of O_3 with alkenes, although this is unlikely to be significant under the relatively clean conditions encountered during NAMBLEX (Salisbury et al., 2001). Figure 7 also clearly demonstrates the general trend for the simple steady state Eq. (4) to over-predict [OH] between 09:00 and 17:00 GMT, where the campaign hourly average calculated/measured ratios varied between 1.00 and 1.69. At these times the majority of OH is formed from primary production which is included in Eq. (4), whereas there are OH sinks, in addition to CO and CH_4, which are not

included in this expression.

5.2.2. Adding other OH sources and sinks to the steady state expression for [OH]

The steady-state prediction of OH levels can be made more realistic through inclusion of additional OH sources and sinks. Equation (4) was extended to include OH production through reaction of HO_2 with NO and with O_3, and OH loss through reaction with *o*-VOCs methanol, acetaldehyde and acetone. These species were selected for inclusion on the basis of Rate of Production Analyses (ROPAs) carried out using the MCM (Sommariva et al., 2005) and by simple kinetic calculations using measured hydrocarbons and *o*-VOCs (Lewis et al., 2005). The ROPAs identified the three main sources of OH, on average, as HO_2+NO (41%), O^1D+H_2O (31%) and HO_2+O_3 (24%). Calculation of the mean pseudo-first-order loss rates for OH due to reactions with various species showed that on average, CO (44%), CH_4 (16%) and *o*-VOCs (including only acetaldehyde, methanol and acetone) (17%) were the major sinks during NAMBLEX, with non-methane hydrocarbons being less important (Read et al., 2003; Lewis et al., 2005). The OH steady-state expression was extended to incorporate these species, resulting in Eq. (11), given below:

$$[\mathrm{OH}]_{ss} = \frac{\mathrm{P(OH)} + X}{k'} \tag{11}$$

where

$$X = (k_{\mathrm{HO_2+O_3}}[\mathrm{O_3}] + k_{\mathrm{HO_2+NO}}[\mathrm{NO}])[\mathrm{HO_2}],$$

and

$$k' = k_{\mathrm{OH+CO}}[\mathrm{CO}] + k_{\mathrm{OH+CH_4}}[\mathrm{CH_4}] + \sum k_{\mathrm{OH+-}o\mathrm{VOCs}}[o\mathrm{VOCs}].$$

The *o*-VOCs included are acetaldehyde, methanol and acetone.

The co-availability of data limited the use of Eq. (11) to 10 days of the campaign, between 10 August and 1 September. Plots of the results of these calculations for the

periods 16–17 and 20–21 August are shown in Fig. 6. The hourly averaged calculated/measured [OH] ratios for the 8 comparison days are shown in Fig. 7. Figure 6 shows that inclusion of additional reactions has made little difference to the calculated/measured [OH] ratios on 17 and 20 August, indicating that the additional sources and sinks are small on these days. However, there are notable differences between [OH] calculated using Eqs. (4) and (11) for 16 and 21 August. Considering the campaign averaged calculated/measured [OH] ratio shown in Fig. 7, the additional OH production terms have resulted in better agreement in the early morning and late afternoon/evening; although there still appears to be a source(s) missing at these times. The photolysis of HONO is a candidate, but as HONO was not measured during NAMBLEX, it is difficult to speculate on this.

On 16 August between 10:00 and 14:00 GMT, the average calculated/measured [OH] ratio increases from an average of 1.10 for calculations made using Eq. (4) to 1.85 for calculations made using Eq. (11), attributed mainly to the addition of the HO_2+NO reaction, which increases the calculated [OH] (NO levels are high and up to 355 pptv). Including the reaction OH+NO_2 (NO_2 levels are up to 690 pptv) as a loss for OH only has a small effect (OH is still over-predicted by an average factor of 1.79 between 10:00–14:00 GMT), suggesting other sinks needs to be included during this polluted period. For 21 August, the shape of the OH profile is calculated more accurately, with a peak in [OH] predicted just before 10:00 GMT when NO, and hence the rate of OH production from the HO_2+NO reaction, is at a maximum. The inclusion of production of OH through HO_2+O_3 and HO_2+NO, and loss of OH through reaction with the *o*-VOCs, has mixed results for the steady-state calculation of [OH].

Figure 7 illustrates that the net effect of the additional source and sinks increases [OH] and hence improves the calculated/measured ratio at the beginning (before 09:00 GMT) and end (after 18:00 GMT) of the day. However, in the middle of the day (between 09:00 and 18:00 GMT), the net effect of additional sources and sinks has worsened the hourly averaged model to measured [OH] ratio, from 1.24±0.62 to 1.38±0.45. Addition of the OH+NO_2 reaction (Fig. 7) improves the agreement by only

~4%, but addition of OH+HCHO leads to a significant improvement (1.24±0.39). See Table 3 for a summary of the results of all steady state [OH] calculations. As mentioned above, non-methane hydrocarbons (NMHC) are not yet included as sinks for OH. Using the campaign averaged concentration of NMHC species measured during NAMBLEX (Lewis et al., 2005, this issue), and with kinetic data taken from Sander et al. (2003) and Atkinson et al. (2002), an average loss rate for OH by reaction with all other hydrocarbons was calculated to be $k'_{HC,\mathrm{tot}}$=0.17 s^{-1} and was included as an OH sink, together with NO_2 and HCHO. Dimethyl sulphide (DMS) and isoprene, which are both highly reactive towards OH, are included in this calculation. Their concentrations displayed a very high variability during the campaign on account of their specific localised sources (Lewis et al., 2005; Heard et al., 2005), and if they are not included as OH sinks $k'_{HC,\mathrm{tot}}$ drops to 0.085 s^{-1}. Inclusion of the additional sinks results in a modified steady-state expression:

$$[\mathrm{OH}]_{ss} = \frac{\mathrm{P(OH)} + X}{k'} \tag{12}$$

where,

$$X = (k_{\mathrm{HO_2+O_3}}[\mathrm{O_3}] + k_{\mathrm{HO_2+NO}}[\mathrm{NO}])[\mathrm{HO_2}]$$

and

$$k' = k_{\mathrm{OH+CO}}[\mathrm{CO}] + k_{\mathrm{OH+CH_4}}[\mathrm{CH_4}] + \sum k_{\mathrm{OH+-}o\mathrm{VOCs}}[o\mathrm{VOCs}] + k_{\mathrm{OH+NO_2}}[\mathrm{NO_2}] + k_{\mathrm{OH+HCHO}}[\mathrm{HCHO}] + k'_{HC_{\mathrm{tot}}}.$$

The results of calculations of [OH] carried out using Eq. (12) are shown in Fig. 7. Inclusion of $k'_{HC,\mathrm{tot}}$ resulted in a further 16% reduction in the calculated/measured [OH] on average, now being 0.94±0.39 for the 8 days (522 data points, 200 s average) for which all measurements were available. If DMS and isoprene are not included, this average ratio is 1.13±0.36. Figure 7 also shows that calculations of [OH] carried out using Eq. (12) are closest in both magnitude and profile shape to measured [OH]. A

summary of the results of all [OH] steady state calculations can be found in Table 3. In Sommariva et al. (2005) of this issue, [OH] is calculated using a box model incorporating the MCM that is constrained by the full suite of measured OH sources and sinks, including halogen species. The period for which OH can be calculated by the full MCM is more limited (availability of data), and the average model/measured [OH] is 1.07±0.64. For the equivalent period the corresponding ratios using Eqs. (4) and (12) are 1.17±0.69 and 1.12±0.53, being within 10 and 5% of the MCM model, respectively. Although the simple expressions perform well, on average, additional OH sources and sinks can sometimes balance one another out, and close agreement with the measured OH may not imply a thorough understanding of the processes controlling the chemistry of OH, and a full mechanism is necessary. Several groups are now directly measuring the total reactivity of OH, k', through its total loss rate in the field, which provides an additional constraint for comparison with models.

5.3. Steady state calculations of HO_2

5.3.1. Solution of the cubic Eq. (5) for the "mini" mechanism

Steady-state HO_2 concentrations can be calculated using the cubic expression (5) (Sect. 2) developed by Carslaw et al. (1999b). In this section we compare observed [HO_2] with those calculated using Eq. (5), and a modified form incorporating the reactions of HO_2 with halogen monoxide species and also loss to aerosol, which have been advanced previously as possible explanations for model overpredictions of HO_2 measurements made in the MBL (Kanaya et al., 2002; Sommariva et al., 2004; Haggerstone et al., 2005). Steady state HO_2 calculations were possible on 9 days of the campaign, maximised by using CO-acetylene and CH_4-propane correlations to fill gaps in CO and CH_4 data. There were also two short intervals for which H_2 measurements were not available, the first from 06:38 GMT 10 August to 15:56 GMT 13 August, and the second from 05:48 GMT 17 August to 14:39 GMT 21 August, for which H_2 levels were interpolated from adjacent measurements (the variation in the mixing ratio of H_2

was small throughout the NAMBLEX campaign with an overall range of 460–610 ppbv). Equation (5) was solved iteratively following computation of the parameters (see Appendix A) from measured co-reactant concentrations (CO, H_2, HCHO, CH_4, NO_2, NO, O_3, P(OH) and j–(HCHO)) and literature rate coefficients. The results of the [HO_2] calculations from four representative days of the campaign (15–16 and 19–20 August) are displayed in Fig. 8, and the hourly averaged calculated/measured HO_2 ratios for 6 days (13, 15–16, 18–21 August) which are used for comparison of calculated [HO_2] throughout Sect. 5.3 are shown as a function of time-of-day in Fig. 9.

Figure 8 illustrates that Eq. (5) (no halogen chemistry or aerosol loss included) significantly overestimates the observed HO_2. Over the 9 days for which calculations of [HO_2] were possible the cubic expression over-predicted HO_2 by an average factor of 4.2±1.6 (1σ). Using co-measurements of IO and BrO made during the NAMBLEX campaign, Bloss et al. (2005a) and Sommariva et al. (2005) have investigated the impact of halogen monoxides on the concentrations of OH and HO_2 through the following reactions:

$$HO_2 + XO \rightarrow HOX + O_2 \quad \text{(R5)}$$

$$HOX + h\nu \rightarrow OH + X \quad \text{(R6)}$$

$$HOX + \text{aerosol} \rightarrow \text{loss} \quad \text{(R7)}$$

Sommariva et al. (2004) and Haggerstone et al. (2005) have examined the impact upon HO_x budgets from the heterogeneous uptake of HO_2 onto aerosols, concluding that the uptake of HO_2 onto sea-salt particles plays a crucial role. During NAMBLEX, IO, BrO, aerosol number density and size distribution were measured together with OH and HO_2 for the first time in the MBL, permitting a more quantitative evaluation of OH and HO_2 budgets.

5.3.2. Impact of halogen monoxides

IO and BrO were measured using long-path Differential Optical Absorption Spectroscopy (DOAS), as described by Saiz-Lopez et al. (2004a, b, 2005a, b). Briefly, the analysis light path was directed from Mace Head to Croaghnakeela Island, 4.2 km offshore to the West of Mace Head, and back via a retro reflector to the receiving telescope and optics, giving a total beam path of 8.4 km, approximately 10 m above sea level. Seven days with 69 hourly averaged IO data points could be matched to the 200 s averaged HO_2 measurements. The loss of HO_2 by reaction with IO was included in the steady-state analysis by adding k_{HO_2+IO} (using $k_{HO_2+IO}=1.4\times10^{-11}\exp^{554/T}$; Knight et al., 2001) to the loss term (B) for calculating β, γ, δ and ε (see Appendix A and Carslaw et al., 1999b, for a full description of the expression and all of its terms). Solution of this modified Eq. (5) results in steady state HO_2 concentrations which reflect the maximum possible effect of the HO_2+IO reaction, as photolysis of the resultant HOI to produce OH, which can then be recycled to HO_2 by reaction with CO and O_3, is not considered. The revised steady-state HO_2 concentrations are shown in Figs. 8 and 9, with inclusion of HO_2+IO significantly reducing the calculated/measured [HO_2] ratio whilst still retaining the shape of the HO_2 diurnal profile. Reductions in the calculated/measured HO_2 ratio compared to the original calculation from Eq. (5) range from 0.5 to 39.1%, with an average of 14±5% (1σ). Despite the significant reduction, there is still a general over-prediction of HO_2, with calculated to measured ratios ranging between 1.0–6.2 with an average of 2.8±0.6 (see Table 4 for a summary of these results).

The above analysis uses IO concentrations averaged over the DOAS beampath. If the principal iodine sources at Mace Head are dominated by local, coastal seaweed emissions of alkyl iodides and molecular iodine, rather than being open ocean in origin, then the IO concentrations at Mace Head may be significantly higher than the beampath average, while those over the open-ocean portion are correspondingly lower. Saiz-Lopez et al. (2005a), provide compelling evidence that the iodine activity is concentrated in a 400 m wide zone next to the shoreline, indicating that the local, Mace

Head IO concentrations are likely to be up to a factor of 10 higher than those returned by the DOAS system. Adding IO concentrations at a level of 10× that measured by DOAS (10×IO) to Eq. (5) resulted in the calculated/measured ratio being decreased by an average of a further 45±7% (1σ), with a calculated/measured HO_2 ratio of between 0.5 and 4.7 with an average of 1.6±0.4 (see Figs. 8 and 9). Thus by including loss of HO_2 by reaction with IO at levels a factor of 10 higher than the DOAS measurements there is a significant improvement in the average calculated/measured HO_2 ratio, although for some time points the increased IO causes the steady state calculations to underpredict HO_2 by as much as 50%. This may arise as a consequence of the omission of the buffering of the additional HO_2 loss through photolysis of HOI, and recycling of the resultant OH to HO_2 via reaction with O_3 and CO. In addition, HO_2 may not be in photochemical equilibrium if the HO_2 lifetime (1–2 min) is comparable with the transport time of the sampled air over the relatively narrow iodine emission region prior to reaching the FAGE instrument. Box model simulations of the impact of IO upon HO_2 during NAMBLEX (Sommariva et al., 2005), found that using 10×IO resulted in good agreement with the measurements on most days.

The conversion of HO_2 to HOI results in an additional source of OH from HOI photolysis. The OH steady state Eq. (11) was modified to include an additional OH production term, accounting for HOI photolysis:

$$\text{Rate of production of OH from HOI photolysis} = (k_{HO_2+IO}[HO_2][IO])\frac{j-(HOI)}{j-(HOI)k'} \qquad (13)$$

where $j-$(HOI) is the rate of photolysis of HOI and k' is the pseudo-first-order rate coefficent for loss of HOI to aerosol, using an HOI uptake coefficient of 0.6 (Sommariva et al., 2005). Including OH production from HOI photolysis increases [OH], averaged over 24 h, by 39%, very similar to the results of Bloss et al. (2005a) and when HOI photolysis is included in the full model (Sommariva et al., 2005). The effect on $[OH]_{ss}$ is dependent on the time of day, being considerably larger early and late in the day, when photolysis of $j-$(HOI) is relatively more important as an OH source when values

of $j-(O^1D)$, and hence P(OH), are reduced. During the middle of the day, 09:00–16:59 GMT, the effect on $[OH]_{ss}$ is on average 23% (20% at noon itself).

The reaction of BrO with HO_2 has the potential to reduce the calculated HO_2 in a qualitatively similar way to IO. DOAS measurements of BrO were made on 6 days of the NAMBLEX campaign, with a maximum daytime concentration of 6.6 pptv seen on 4 August. (Saiz-Lopez et al., 2004b). Matching of the 63 hourly averaged BrO data points to the 200 s HO_2 data allowed HO_2 to be calculated using Eq. (5), modified to include the HO_2+BrO with k_{HO_2+BrO} (Bloss et al., 2002; Sander et al., 2003), although HO_2 measurements were only made on one of these, namely 10 August. On this day the calculated/measured HO_2 ratio was seen to decrease by between 1.8 and 10.5% with an average reduction of 6.2% compared to the original calculations of $[HO_2]$ carried out using Eq. (5) (excluding BrO). Again, these calculations only demonstrate the maximum possible effect of loss of HO_2 via reaction with BrO, as we have assumed that all HOBr is lost onto aerosols and that none is photolysed. This assumption is more valid in the case of HOBr than for HOI, as the rate of photolysis of HOBr is a factor of 4.5 lower than that for HOI. The lower rate of photolysis of HOBr results in a reduced buffering of the HO_2 loss through the recycling of the resultant OH (by reaction with O_3 and CO) compared to that seen through photolysis of HOI.

5.3.3. Impact of HO_2 uptake to aerosol

Another possible cause for over-prediction of the observed HO_2 levels is the omission of the uptake of HO_2 onto aerosol. The lifetime of HO_2 in the clean MBL air is of the order of 1–2 min, and so the heterogeneous uptake of HO_2 onto aerosols has the potential to significantly influence the HO_x budget. During NAMBLEX, detailed measurements of the size-dependent chemical and physical properties of particles were made (Coe et al., 2005) and these data were used to calculate pseudo-first-order rate coefficients for the uptake of HO_2 onto aerosol particles (Sander, 1999; Haggerstone et al., 2005; Sommariva et al., 2005; Bloss et al, 2005a). HO_2 aerosol

uptake rates ($k'_{aerosol}$) were derived from ambient humidity aerosol size distributions (from 3 nm to 30 microns, assembled from a combination of mobility, backscatter and forward scattering measurements) considering mass transfer in the transition regime, and using a reaction probability of γ=1.0, i.e. the upper limit for loss of HO_2. There is a large variation in the available literature values for the HO_2 uptake coefficient upon wet sea-salt aerosol, leading to a large source of uncertainty in the calculated rate of HO_2 uptake. Here we only consider the maximum possible reduction in [HO_2] by including aerosol uptake by using values of $k'_{aerosol}$ calculated from an uptake coefficient of unity. The HO_2 loss term used to calculate β, γ, δ, and ε (see Appendix A) was modified using 1475 $k'_{aerosol}$ data points calculated on a 30 min time basis and matched to the 200 s HO_2 measurements.

The effect of including aerosol uptake is shown on Figs. 8 and 9. There is a significant reduction in the calculated/measured HO_2 ratio, ranging from 12 to 72% with an average reduction of 38±12% (1σ) compared to the original calculations using Eq. (5). Similar to the results found for addition of the HO_2+IO reaction to Eq. (5), it is clear that uptake of HO_2 onto aerosols alone cannot account for the over-prediction of HO_2, with an overall mean HO_2 calculated/measured ratio of 2.0±0.7 (1σ). The exception occurs on the morning of 16 August when the addition of uptake of HO_2 onto aerosols to Eq. (5) results in an average calculated/measured HO_2 ratio of 1.0±0.3 (1σ) between 06:40 and 09:03 GMT. The addition of uptake of HO_2 onto aerosols generally causes a greater reduction in the calculated/measured [HO_2] ratio than that seen on addition of the HO_2+IO reaction, the exception to this being on 18 August when the campaign maximum IO were measured (up to 5 pptv). Inclusion of the uptake of HO_2 onto aerosols in Eq. (5) causes an average of an additional 23% reduction in the calculated/measured [HO_2] ratio compared to that found on inclusion of HO_2+IO. Uptake of HO_2 onto aerosols appears to play an important role in the free-radical chemistry of the MBL, but further studies of the physical and chemical properties of aerosols and, in particular, the rate coefficients for the heterogeneous uptake of HO_2 radicals onto realistic aerosol surfaces are required to further our understanding of the HO_x cycle in

this environment.

5.3.4. Combined effect of halogen oxides and aerosol uptake upon HO_2

In the two preceding subsections it was shown that the reaction of HO_2 with IO or the uptake of HO_2 onto aerosols cannot in isolation account for the over-prediction of HO_2 when using Eq. (5). Hence, in an attempt to more accurately predict HO_2, both loss mechanisms were included in Eq. (5), and HO_2 was recalculated in the manner described above. This allowed calculations of HO_2 to be made on 6 days of the campaign, several examples of which are shown in Fig. 8, with the hourly average calculated/measured [HO_2] ratios for the 6 comparable days in Fig. 9. Addition of both loss of HO_2 via reaction with IO (using DOAS measured values) and uptake onto aerosols resulted in reductions in the calculated/measured HO_2 ratio of between 13 and 72%, with an average reduction of 43±10% (1σ) compared to the original calculations carried out using Eq. (5). However, even with the cumulative effects of the addition of both loss of HO_2 *via* reaction with IO and uptake onto aerosols the modified Eq. (5) still over-predicts the observed HO_2 by a factor of 1.9±0.6 (1σ). It is only on addition of both IO×10 and uptake of HO_2 onto aerosols that agreement (within uncertainty) between the calculated and measured HO_2 concentrations is achieved, with an average calculated/measured ratio of 1.3±0.4 (1σ).

In order to consider the additional reduction in the calculated HO_2 levels due to reaction with BrO in addition to reaction with IO and heterogeneous uptake, it was necessary to determine typical BrO levels (simultaneous DOAS measurements of IO and BrO were not possible due to the different spectral ranges of their principal absorption features). Hourly averages of BrO between 10:00 and 14:00 GMT were determined over the whole campaign, and were used along with the hourly averages of all other necessary parameters for the 6 comparable days in order to calculate new values for β, γ, δ, and ε such that loss of HO_2 via reaction with IO, BrO and uptake onto aerosols were included in Eq. (5). Using these typical BrO levels it was found that inclusion of the reaction of HO_2+BrO only reduced the calculated/measured [HO_2] ratio by a fur-

ther 3.1±1.0% (1σ) on average. The results of calculations of HO_2 using Eq. (5) with various loss schemes are summarised in Table 4.

In Sommariva et al. (2005) of this issue a box model using the MCM was used to calculate [HO_2]. Using a scheme which does not include halogens/aerosol uptake the modelled/measured HO_2 ratio is 2.43±0.82, averaged between 15 and 20 August, which improves to 1.09±0.42 if uptake to aerosol (γ=1.0) and the reaction HO_2+IO is included.

6. Discussion

6.1. HO_x observations

Concentrations of OH measured during NAMBLEX are in good agreement with those measured previously at Mace Head (Creasey et al., 1997, 2002, and Berresheim et al., 2002), although significantly lower than the levels observed by Berresheim et al. (2003) at a coastal site in Crete during the MINOS campaign, where levels of NO_x were considerably higher. There was a good correlation between [OH] and $j(O^1D)$ (Fig. 2), but not as good as observed during MINOS or SOAPEX-2 (Cape Grim, Creasey et al., 2003), because of more short-term variability in the OH concentrations, probably due to more local variability in co-reactant concentrations at the Mace Head site. The 24 h average OH concentration, 9.1×10^5 molecule cm^{-3}, agrees well with estimates for the northern hemisphere troposphere derived from methyl chloroform data (e.g. Prinn et al., 2001; mean OH=$(8.98\pm2.02)\times10^5$ molecule cm^{-3}).

The daytime HO_2 levels were also comparable with those measured previously at Mace Head (e.g. Creasey et al., 2002). Measurements of total [RO_2] by the PERCA (Peroxy Radical Chemical Amplifier) technique during NAMBLEX indicated that HO_2 comprised between 20 and 40% of the total RO_2 radicals during the daytime, falling to ca. 15% overnight. The RO_2 radical measurements, and specifically the HO_2/total RO_2 ratio, are described in more detail in Fleming et al. (2005).

6.2. OH steady-state analysis

The gross features of the dataset of OH concentrations could be replicated using a very simple steady-expression incorporating only primary production from ozone photolysis and loss by reaction with CH_4 and CO. Including the reactions of HO_2 with NO and O_3 as an OH source and the reactions of OH with *o*-VOCs, HCHO, NO_2 and non-methane hydrocarbons improved the agreement, with an average calculated to measured OH concentration of 0.94±0.39 (1.13±0.36 if isoprene and DMS are not included). This ratio is consistent with the value of 1.07±0.64 obtained using the box model employing the MCM (Sommariva et al., 2005), and also with the predictions of a global chemistry-transport model (GEOS-CHEM), which overestimated the observed OH by 25% for the NAMBLEX campaign (Bloss et al., 2005b). Despite the average ratio being close to unity, examination of Fig. 7 clearly shows that the calculated to modelled OH ratio displays a considerable diurnal variation, with steady state calculations underestimating OH in the early morning and evenings, and overestimating OH during the middle of the day. The overestimation is not too surprising as not all OH sinks are included in the steady-state expression. The underprediction at higher SZA suggests that other sources are missing in the analysis, for example photolysis of suitable precursors at longer wavelengths than required for O_3 photolysis. The reaction of O_3 with alkenes is not a significant source of daytime HO_x under the relatively clean conditions experienced during NAMBLEX (Sommariva et al., 2005). HONO was not measured, and so the net result of HONO photolysis to give OH and its formation from the OH+NO+M reaction has not been evaluated but under the predominantly low NO_x environment of Mace Head is not expected to be significant source of OH (Carslaw et al., 2002).

6.3. HO_2 steady-state analysis

Using HO_2 data from the NAMBLEX campaign we have been able to test the ability of a cubic expression, Eq. (5), derived using a reduced mechanism of an MCM model tailored to conditions at Mace Head (Carslaw et al., 1999b), to predict HO_2. The cal-

culations are able to capture the general features of the HO_2 diurnal profiles, but fail to accurately predict the absolute concentration of HO_2, with a mean calculated to observed [HO_2] ratio of 3.22±0.69. Addition of HO_2 sinks in the form of reaction with IO and uptake onto aerosols reduces this value to 1.87±0.61 for the 6 days over which co-reactant data were available. Including loss of HO_2 by reaction with 10 times the IO measured by DOAS, accounting for the non-uniform distribution of iodine species thought to be present along the DOAS beampath at Mace Head (Saiz-Lopez et al., 2005a), together with uptake of HO_2 onto aerosols, gave a further agreement to give a ratio of 1.29±0.36. The analysis does not include buffering of the loss of HO_2 through photolysis of HOI (formed by HO_2+IO) and recycling of the resultant OH through reaction with O_3 and CO back to HO_2. In this manner OH could be increased on average by 43% in the early morning/late afternoon and on average by 23% in the middle of the day. Also, the fetch over the shoreline region which acts as the major iodine source is of the order of 400 m and transport times over this region may be comparable to the lifetime of HO_2 (1–2 min), and thus HO_2 may not be in photochemical steady state, as is assumed in the derivation of Eq. (5).

7. Conclusions

OH and HO_2 radicals have been measured at the Mace Head Atmospheric Research Station during July and August 2002 by laser induced fluorescence. OH was measured on 24 days and showed a distinct diurnal profile, strongly correlated with $j-(O^1D)$, with maximum OH concentrations observed at noon of $(3–8)\times10^6$ molecule cm^{-3}. HO_2 was observed on 17 days, with maximum mixing ratios in the range 3.5–8 pptv. A simple steady-state expression was used to calculate OH which included loss by reaction with CO, CH_4, HCHO, NO_2, methanol, acetaldehyde, acetone and an average total loss by reaction with non-methane hydrocarbons, and production by O_3 photolysis and the reactions of HO_2 with NO and O_3. An average ratio of OH calculated using this expression to measured OH was 0.94±0.39. Inclusion of the oxygenated species, which

had not been previously measured at Mace Head, improved the agreement considerably. Although the average ratio is close to unity, the ratio displayed a distinct diurnal variation, with the model overpredicting in the middle of the day and underpredicting in the early morning and late afternoon/evening. HO_2 concentrations were calculated using a cubic equation which is an analytic solution to a simple chemical mechanism previously developed for the remote MBL. The calculation overestimates HO_2, but the agreement with measurement is improved considerably by the inclusion of heterogeneous loss of HO_2 to aerosol, and reaction of HO_2 with the halogen oxides IO and BrO giving a calculated/measured $[HO_2]$ ratio of 1.29±0.36.

Appendix A

As discussed in Carslaw et al. (1999b, 2002), a reduced "mini" mechanism, consisting of 25 reactions and 17 species, leads to the following cubic equation for the concentration of HO_2:

$$\beta[HO_2]^3 + \gamma[HO_2]^2 + \delta[HO_2] + \varepsilon = 0 \tag{A1}$$

where,

$$\beta = 2k_{T2}(k_{T3}B + k_{T1}A) \tag{A2}$$

$$\gamma = 2k_{T3}k_{T2}J_1 + 2k_{T3}k_{p5}[NO]B + 2k_{T2}k_{p4}[CH_4]B + k_T[NO_2]k_{T2}B + 2Ak_{T1}k_{p5}[NO] \tag{A3}$$

$$\delta = 2k_{T3}k_{p5}J_1[NO] + 2k_{T2}k_{p4}J_1[CH_4] + k_TJ_1[NO_2]k_{T2} + k_TB[NO_2]k_{p5}[NO] - (J_1 + J_2)Ak_{T2} \tag{A4}$$

$$\varepsilon = J_1k_T[NO_2]k_{p5}[NO] - (J_1 + J_2)Ak_{p5}[NO] \tag{A5}$$

where,

$$J_1 = \mathrm{P(OH)} = 2f[\mathrm{O_3}]j - (\mathrm{O^1D}) \quad \text{(A6)}$$

$$J_2 = 2j - (\mathrm{HCHO} \rightarrow 2\mathrm{HO_2})[\mathrm{HCHO}] \quad \text{(A7)}$$

$$A = k_{\mathrm{CO+OH}}[\mathrm{CO}] + k_{\mathrm{H_2+OH}}[\mathrm{H_2}] + k_{\mathrm{HCHO+OH}}[\mathrm{HCHO}] + k_{\mathrm{CH_4+OH}}[\mathrm{CH_4}] + k_{\mathrm{NO_2+OH}}[\mathrm{NO_2}] + k_{\mathrm{O_3+OH}}[\mathrm{O_3}] \quad \text{(A8)}$$

$$B = k_{\mathrm{HO_2+NO}}[\mathrm{NO}] + k_{\mathrm{HO_2+O_3}}[\mathrm{O_3}] \quad \text{(A9)}$$

$$k_T = k_{\mathrm{OH+NO2}} \quad \text{(A10)}$$

$$k_{T1} = k_{\mathrm{HO_2+HO_2}} \quad \text{(A11)}$$

$$k_{T2} = k_{\mathrm{HO_2+CH_3O_2}} \quad \text{(A12)}$$

$$k_{T3} = k_{\mathrm{OH+HO_2}} \quad \text{(A13)}$$

$$k_{p4} = k_{\mathrm{CH_4+OH}} \quad \text{(A14)}$$

$$k_{p5} = k_{\mathrm{CH_3O_2+NO}} \quad \text{(A15)}$$

Acknowledgements. Thanks are given to T. Ingham for assistance with the development of the FAGE instrument, and to K. Read for assistance with the preparation of this manuscript. We are also grateful to the other participants of NAMBLEX for providing data used in the analysis and interpretation of OH and HO_2 measurements. We are grateful to the NERC for funding this work under grant number NER/A/S/2000/01313.

References

Atkinson, R., Baulch, D. L., Cox, R. A., Crowley, J. N., Hampson, R. F., Kerr, J. A., Rossi, M., and Troe, J.: Summary of evaluated kinetic and photochemical data for atmospheric chemistry, see http://www.iupac-kinetic.ch.cam.ac.uk/, 2002.

Berresheim, H., Elste, T., Tremmel, H. G., Allen, A. G., Hansson, H. C., Rosman, K., Dal Maso, M., Makela, J. M., Kulmala, M., and O'Dowd, C. D.: Gas-aerosol relationships of H_2SO_4, MSA, and OH: Observations in the coastal marine boundary layer at Mace Head, Ireland, J. Geophys. Res.-Atmos., 107(D19), art. no. 8100, doi:10.1029/2000JD000229, 2002.

Berresheim, H., Plass-Dulmer, C., Elste, T., Mihalopoulos, N., and Rohrer, F.: OH in the coastal boundary layer of Crete during MINOS: Measurements and relationship with ozone photolysis, Atmos. Chem. Phys., 3, 639–649, 2003, SRef-ID: 1680-7324/acp/2003-3-639.

Bloss, W. J., Evans, M. J., Lee, J. D., Sommariva, R., Heard, D. E., and Pilling, M. J.: The oxidative capacity of the troposphere: Coupling of field measurements of OH and a global chemistry transport model, Faraday Discuss., 130, 425–436, 2005b.

Bloss, W. J., Gravestock, T. J., Heard, D. E., Ingham, T., Johnson, G. P., and Lee, J. D.: Application of a compact all solid-state laser system to the in situ detection of atmospheric OH, HO_2, NO and IO by laser-induced fluorescence, J. Environ. Monitoring, 5, 21–28, 2003.

Bloss, W. J., Lee, J. D., Johnson, G. P., Sommariva, R., Heard, D. E., Saiz-Lopez, A., Plane, J. M. C., McFiggans, G., Coe, H., Flynn, M., Williams, P., Rickard, A. R., and Fleming, Z. L.: Impact of halogen monoxide chemistry upon boundary layer OH and HO_2 concentrations at a coastal site, Geophys. Res. Lett., 32, L06814, doi:10.1029/2004GL022084, 2005a.

Bloss, W. J., Rowley, D. M., Cox, R. A., and Jones, R. L.: Rate coefficient for the BrO + HO_2 reaction at 298 K, Phys. Chem. Chem. Phys., 4 (15), 3639–3647, 2002.

Brauers, T., Hausmann, M., Bister, A., Kraus, A., and Dorn, H. P.: OH radicals in the boundary layer of the Atlantic Ocean 1. Measurements by long-path laser absorption spectroscopy, J. Geophys. Res.-Atmos., 106(D7), 7399–7414, 2001.

Cantrell, C. A., Tyndall, G., and Zimmer, A.: Absorption cross sections for water vapour from 183 to 193 nm, Geophys. Res. Lett., 24, 2195–2198, 1997.

Cape, J. N., Methven, J., and Hudson, L. E.: The use of trajectory cluster analysis to interpret trace gas measurements at Mace Head, Ireland, Atmos. Environ., 34, 3651–3663, 2000.

Carslaw, N., Creasey, D. J., Heard, D. E., Jacobs, P. J., Lee, J. D., Lewis, A. C., McQuaid,

J. B., Pilling, M. J., Bauguitte, S., Penkett, S. A., Monks, P. S., and Salisbury, G.: Eastern Atlantic Spring Experiment 1997 (EASE97) – 2. Comparisons of model concentrations of OH, HO_2, and RO_2 with measurements, J. Geophys. Res.-Atmos., 107(D14), art. no. 4190, doi:10.1029/2001JD001568, 2002.

Carslaw, N., Creasey, D. J., Heard, D. E., Lewis, A. C., McQuaid, J. B., Pilling, M. J., Monks, P. S., Bandy, B. J., and Penkett, S. A.: Modelling OH, HO_2, and RO_2 radicals in the marine boundary layer – 1. Model construction and comparison with field measurements, J. Geophys. Res.-Atmos., 104(D23), 30 241–30 255, 1999a.

Carslaw, N., Jacobs, P. J., and Pilling, M. J.: Modelling OH, HO_2, and RO_2 radicals in the marine boundary layer – 2. Mechanism reduction and uncertainty analysis, J. Geophys. Res.-Atmos., 104(D23), 30 257–30 273, 1999b.

Chen, G., Davis, D., Crawford, J., Heikes, B., O'Sullivan, D., Lee, M., Eisele, F., Mauldin, L., Tanner, D., Collins, J., Barrick, J., Anderson, B., Blake, D., Bradshaw, J., Sandholm, S., Carroll, M., Albercook, G., and Clarke, A.: An assessment of HO_x chemistry in the tropical Pacific boundary layer: Comparison of model simulations with observations recorded during PEM tropics A, J. Atmos. Chem., 38 (3), 317–344, 2001.

Coe, H., Allan, J., Alfarra, M., Bower, K., Flynn, M., McFiggans, G., Topping, D., Williams, P., Dall'Osto, M., Beddows, D., and Harrison, R.: Chemical and Physical Characteristics of Aerosol Particles at a remote coastal location, Mace Head, Ireland, during NAMBLEX, Atmos. Chem. Phys. Discuss., accepted, 2005.

Creasey, D. J., Evans, G. E., Heard, D. E., and Lee, J. D.: Measurements of OH and HO_2 concentrations in the Southern Ocean marine boundary layer, J. Geophys. Res.-Atmos., 108(D15), 4475, doi:10.1029/2002JD003206, 2003.

Creasey, D. J., HalfordMaw, P. A., Heard, D. E., Pilling, M. J., and Whitaker, B. J.: Implementation and initial deployment of a field instrument for measurement of OH and HO_2 in the troposphere by laser-induced fluorescence, J. Chem. Soc.-Faraday Trans., 93 (16), 2907–2913, 1997.

Creasey, D. J., Halford-Maw, P. A., Heard, D. E., Spence, J. E., and Whitaker, B. J.: Fast photomultiplier tube gating system for photon counting applications, Rev. Sci. Instr., 69 (12), 4068–4073, 1998.

Creasey, D. J., Heard, D. E., and Lee, J. D.: Absorption cross-section measurements of water vapour and oxygen at 185 nm. Implications for the calibration of field instruments to measure OH, HO_2 and RO_2 radicals, Geophys. Res. Lett., 27(11), 1651–1654, 2000.

Creasey, D. J., Heard, D. E., and Lee, J. D.: Eastern Atlantic Spring Experiment 1997 (EASE97) 1. Measurements of OH and HO_2 concentrations at Mace Head, Ireland, J. Geophys. Res.-Atmos., 107(D10), art. no. 4091, doi:10.1029/2001JD000892, 2002.

Ehhalt, D. H. and Rohrer, F.: Dependence of the OH concentration on solar UV, J. Geophys. Res.-Atmos., 105, 3565–3571, 2000.

Fleming, Z., Monks, P. S., Rickard, A. R., Heard, D. E., Still, T. J., Sommariva, R., Pilling, M. J., Green, T., Brough, N., Penkett, S. A., Lewis, A. C., Lee, J. D., Saiz-Lopez, A., and Plane, J. M. C.: Peroxy Radical Chemistry and the Control of Ozone Photochemistry at Mace Head, Ireland during the Summer of 2002, Atmos. Chem. Phys. Discuss., accepted, 2005.

Haggerstone, A. L., Carpenter, L. J., Carslaw, N., and McFiggans, G.: Improved model predictions of HO_2 with gas to partical mass transfer rates calculated using aerosol number size distibutions, J. Geophys. Res.-Atmos., 110, doi:10.1029/2004JD005282, 2005.

Hard, T. M., O'Brien, R. J., Chan, C. Y., and Mehrabzadeh, A. A.: Tropospheric Free-Radical Determination by FAGE, Environ. Sci. Technol., 18 (10), 768–777, 1984.

Heard, D. E. and Pilling, M. J.: Measurement of OH and HO_2 in the troposphere, Chem. Rev., 103, 5163–5198, 2003.

Heard, D. E., Read, K. A., Methven, J., et al.: The North Atlantic Marine Boundary Layer Experiment (NAMBLEX). Overview of the campaign held at Mace Heard, Ireland, in summer 2002, Atmos. Chem. Phys. Discuss., in press, 2005.

Hofzumahaus, A., Brauers, T., Aschmutat, U., Brandenburger, U., Dorn, H. P., Hausmann, M., Hessling, M., Holland, F., PlassDulmer, C., Sedlacek, M., Weber, M., and Ehhalt, D. H.: The measurement of tropospheric OH radicals by laser-induced fluorescence spectroscopy during the POPCORN field campaign and intercomparison of tropospheric OH radical measurements by multiple folded long-path laser absorption and laser induced fluorescence – Reply, Geophys. Res. Lett., 24(23), 3039–3040, 1997.

Holland, F., Hessling, M., and Hofzumahaus, A.: In-situ measurement of tropospheric OH radicals by laser-induced fluorescence – a description of the KFA instrument, J. Atmos. Sci., 52 (19), 3393–3401, 1995.

Jenkin, M. E., Saunders, S. M., and Pilling, M. J.: The tropospheric degradation of volatile organic compounds: A protocol for mechanism development, Atmos. Environ., 31, 81–104, 1997.

Kanaya, Y., Matsumoto, J., Kato, S., and Akimoto, H.: Behavior of OH and HO_2 radicals during the Observations at a Remote Island of Okinawa (ORION99) field campaign 2. Comparison

between observations and calculations, J. Geophys. Res.-Atmos., 106(D20), 24 209–24 223, 2001a.

Kanaya, Y., Sadanaga, Y., Hirokawa, J., Kajii, Y., and Akimoto, H.: Development of a ground-based LIF instrument for measuring HO_x radicals: Instrumentation and calibrations, J. Atmos. Chem., 38 (1), 73–110, 2001b.

Kanaya, Y., Yokouchi, Y., Matsumoto, J., Nakamura, K., Kato, S., Tanimoto, H., Furutani, H., Toyota, K., and Akimoto, H.: Implications of iodine chemistry for daytime HO_2 levels at Rishiri Island, Geophys. Res. Lett., 29(8), art. no. 1212, doi:10.1029/2001GL014061, 2002.

Levy, H.: Normal atmosphere: large radical and formaldehyde concentrations predicted, Science, 173, 141–143, 1971.

Lewis, A. C., Hopkins, J. R., Carpenter, L.J., Stanton, J., Read, K. A., and Pilling, M. J.: Sources and sinks of acetone, methanol, and acetaldehyde in North Atlantic marine air, Atmos. Chem. Phys., 5, 1963–1974, 2005, SRef-ID: 1680-7324/acp/2005-5-1963.

Logan, J. A., Prather, M. J., Wofsy, S. C., and McElroy, M. B.: Tropospheric chemistry: A global perspective, J. Geophys. Res., 86, 7210–7254, 1981.

Norton, E. G., Vaughan, G., Methven, J., Coe, H., Brooks, B., Gallagher, M., and Longley, I.: Boundary layer structure and decoupling from synoptic scale flow during NAMBLEX, Atmos. Chem. Phys. Discuss., 5, 3191–3223, 2005, SRef-ID: 1680-7375/acpd/2005-5-3191.

Penkett, S. A., Monks, P. S., Carpenter, L. J., Clemitshaw, K. C., Ayers, G. P., Gillett, R. W., Galbally, I. E., and Meyer, C. P.: Relationships between ozone photolysis rates and peroxy radical concentrations in clean marine air over the Southern Ocean, J. Geophys. Res.-Atmos., 102(11D), 12 805–12 817, 1997.

Prinn, R. G., Huang, J., and Weiss, R. F.: Evidence for substantial variations of atmospheric hydroxyl radicals in the past two decades, Science, 292, 1882–1888, 2001.

Read, K. A., Hopkins, J. R., and Lewis, A. C.: Low molecular weight organic compounds in maritime air: Recent results from the NAMBLEX experiment, EGS-AGU-EGU General Assembly, Nice, 2003.

Saiz-Lopez, A. and Plane, J. M. C.: Novel iodine chemistry in the marine boundary layer, Geophys. Res. Lett., 31, L04112, doi:10.1029/2003GL019215, 2004a.

Saiz-Lopez, A., Plane, J. M. C., and Shillito, J. A.: Bromine oxide in the mid-latitude marine boundary layer, Geophys. Res. Lett., 31(3), L03111, doi:10.1029/2003GL018956, 2004b.

Saiz-Lopez, A., Plane, J. M. C., McFiggans, G., Ball, S. M., Bitter, M., Jones, R. L., Hongwei, C., and Hoffmann, T.: Modelling molecular iodine emissions in a coastal marine environment: the link to particle formation, Atmos. Chem. Phys. Discuss., 5, 5405–5439, 2005a, SRef-ID: 1680-7375/acpd/2005-5-5405.

Saiz-Lopez, A., Shillito, J. A., Coe, H., and Plane, J. M. C.: Measurements and modelling of I_2, IO, OIO, BrO and NO_3 in the mid-latitude marine boundary layer, Atmos. Chem. Phys. Discuss., 5, 9731–9767, 2005b, SRef-ID: 1680-7375/acpd/2005-5-9731.

Salisbury, G., Rickard, A. R., Monks, P. S., Allan, B. J., Bauguitte, S., Penkett, S. A., Carslaw, N., Lewis, A. C., Creasey, D. J., Heard, D. E., Jacobs, P. J., and Lee, J. D.: Production of peroxy radicals at night via reactions of ozone and the nitrate radical in the marine boundary layer, J. Geophys. Res.-Atmos., 106(D12), 12 669–12 687, 2001.

Sander, R.: Modelling atmospheric chemistry: Interactions between gas-phase species and the liquid cloud/aerosol particles, Surveys in Geophysics, 20 (1), 1–31, 1999.

Sander, S. P., Friedl, R. R., Golden, D. M., Kurylo, M. J., Huie, R. E., Orkin, V. L., Moorgat, G. K., Ravishankara, A. R., Kolb, C. E., Molina, L. T., and Finlayson-Pitts, B. J.: Chemical kinetics and photochemical data for use in atmospheric studies: Evaluation number 14, JPL publication 02-25, 2003.

Schultz, M., Heitlinger, M., Mihelcic, D., and Volzthomas, A.: Calibration source for peroxy-radicals with built-in actinometry using H_2O and O_2 photolysis at 185 nm, J. Geophys. Res.-Atmos., 100(D9), 18 811–18 816, 1995.

Simmonds, P. G., Derwent, R. G., McCulloch, A., Odoherty, S., and Gaudry, A.: Long-term trends in concentrations of halocarbons and radiatively active trace gases in Atlantic and European air masses monitored at Mace Head, Ireland from 1987–1994, Atmos. Environ., 30 (23), 4041–4063, 1996.

Sommariva, R., Bloss, W. J., Brough, N., Carslaw, N., Flynn, M., Haggerstone, A. L., Heard, D. E., Hopkins, J. R., Lee, J. D., Lewis, A. C., McFiggans, G., Monks, P. S., Penkett, S. A., Pilling, M. J., Plane, J. M. C., Read, K. A., Saiz-Lopez, A., Rickard, A. R., and Williams, P. I.: OH and HO_2 chemistry during NAMBLEX: Roles of oxygenates, halogen oxides and heterogeneous uptake, Atmos. Chem. Phys. Discuss., 5, 10 947–10 996, 2005a, SRef-ID: 1680-7375/acpd/2005-5-10947.

Sommariva, R., Haggerstone, A. L., Carpenter, L. J., Creasey, D. J., Carslaw, N., Heard, D. E., Lee, J. D., Lewis, A. C., Pilling, M. J., and Zador, J.: OH and HO_2 chemistry in clean marine

air during SOAPEX-2, Atmos. Chem. Phys., 4, 839–856, 2004, SRef-ID: 1680-7324/acp/2004-4-839.

Stevens, P. S., Mather, J. H., and Brune, W. H.: Measurement of tropospheric OH and HO_2 by laser-induced fluorescence at low-pressure, J. Geophys. Res.-Atmos., 99(D2), 3543–3557, 1994.

Table 1. Fitting Eq. (10) to OH/j–(O^1D) data for the entire campaign, uncertainties are $\pm 1\sigma$.

Fit	a	b	c	r^2
1 Linear	1.67±0.02	1 (fixed)	0 (fixed)	0.404
2 Power	1.98±0.02	0.59±0.02	0 (fixed)	0.470
3 Power/Intercept	1.47±0.08	0.84±0.05	0.44±0.06	0.476

Table 2. Results of fitting Eq. (10) to OH/$j-(O^1D)$ data sorted into NO bins i) NO=0–10 pptv, ii) NO=10–30 pptv, iii) NO=30–500 pptv.

Fit	a	b	c	r^2
i)				
1 Linear	1.43±0.03	1 (fixed)	0 (fixed)	0.519
2 Power	1.64±0.05	0.71±0.05	0 (fixed)	0.593
3 Power/Intercept	0.81±0.09	1.51±0.14	0.58±0.06	0.576
ii)				
1 Linear	1.68±0.02	1 (fixed)	0 (fixed)	0.462
2 Power	1.90±0.03	0.68±0.03	0 (fixed)	0.496
3 Power/Intercept	1.11±0.09	1.22±0.09	0.64±0.07	0.515
iii)				
1 Linear	1.89±0.04	1 (fixed)	0 (fixed)	0.389
2 Power	2.29±0.04	0.56±0.03	0 (fixed)	0.509
3 Power/Intercept	2.38±0.33	0.54±0.09	−0.08±0.30	0.509

Table 3. The range, mean and 1σ standard deviations in the calculated/measured [OH] ratios for calculations carried out with Eq. (4), Eq. (11) with various modifications to include loss of OH to NO_2 and both NO_2 and HCHO and Eq. (12). All the data shown are from calculated from 522 data points (200 s average) on 8 days (10 and 15–21 August).

	Lower	Upper	Mean	St Dev
Eq. (4)	0.01	11.07	1.24	0.62
Eq. (11)	0.12	10.90	1.38	0.45
Eq. (11) inc OH+NO_2	0.11	10.83	1.34	0.46
Eq. (11) inc OH+NO_2 and OH + HCHO	0.11	9.55	1.24	0.39
Eq. (12)	0.09	7.93	0.94	0.39
Eq. (12) excluding isoprene and DMS	0.10	8.68	1.13	0.36

Table 4. The range, mean and 1σ standard deviations in the calculated/measured [HO_2] ratios for calculations using Eq. (5) with various modifications to include loss of HO_2 to: IO, IO×10, uptake onto aerosol (γ_{HO_2}=1.0), IO + uptake onto aerosol (γ_{HO_2}=1.0) and IO×10 + uptake onto aerosol (γ_{HO_2}=1.0). All the data shown are calculated from 281 data points (200 s average) on 6 days (13, 15–16 and 18–21 August).

	Lower	Upper	Mean	St Dev
Eq. (5)	1.16	6.93	3.22	0.69
Eq. (5) + IO	1.00	6.17	2.79	0.57
Eq. (5) + (IO×10)	0.46	4.68	1.60	0.39
Eq. (5) + aerosols	0.47	5.27	2.03	0.71
Eq. (5) + IO + aerosols	0.46	4.9	1.87	0.61
Eq. (5) + IO×10 + aerosols	0.35	4.74	1.29	0.36

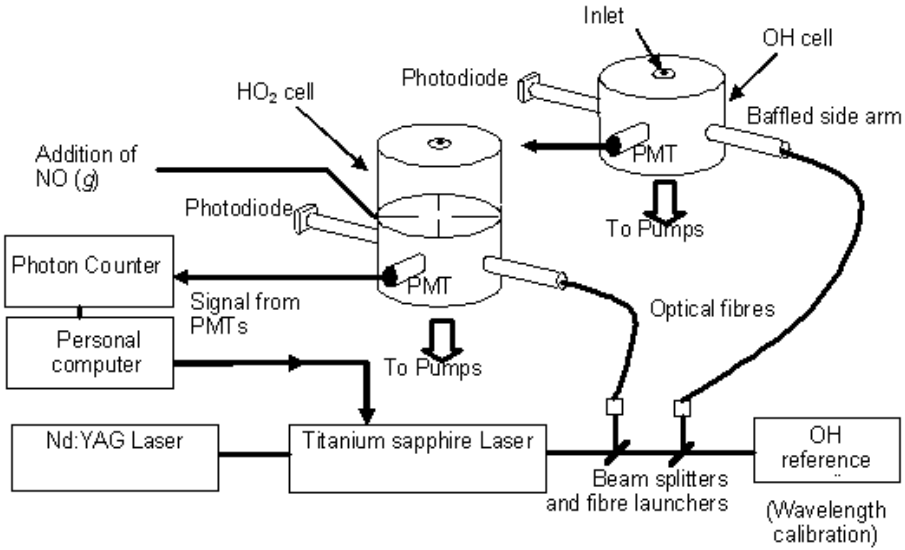

Fig. 1. A schematic of the FAGE instrument as deployed during the NAMBLEX campaign.

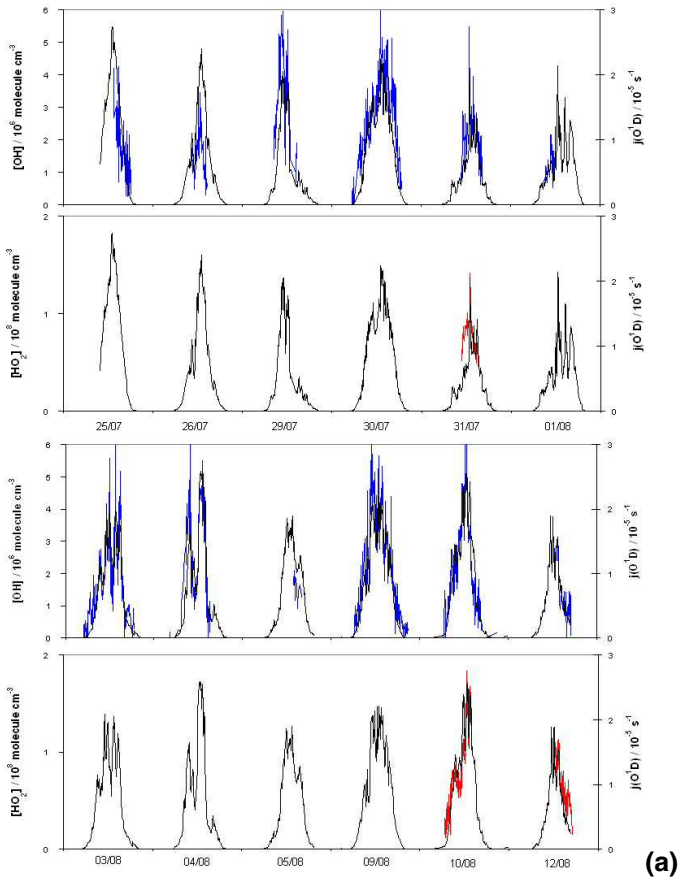

Fig. 2. Time-series of OH (blue) and HO_2 (red) concentrations during NAMBLEX. Each point represents a 5 min collection period comprising 10 adjacent 20 s online data points with a consecutive background period consisting of 5 adjacent 20 s data points. 5 min averaged $j-(O^1D)$ (black) as measured by a spectral radiometer, are also shown.

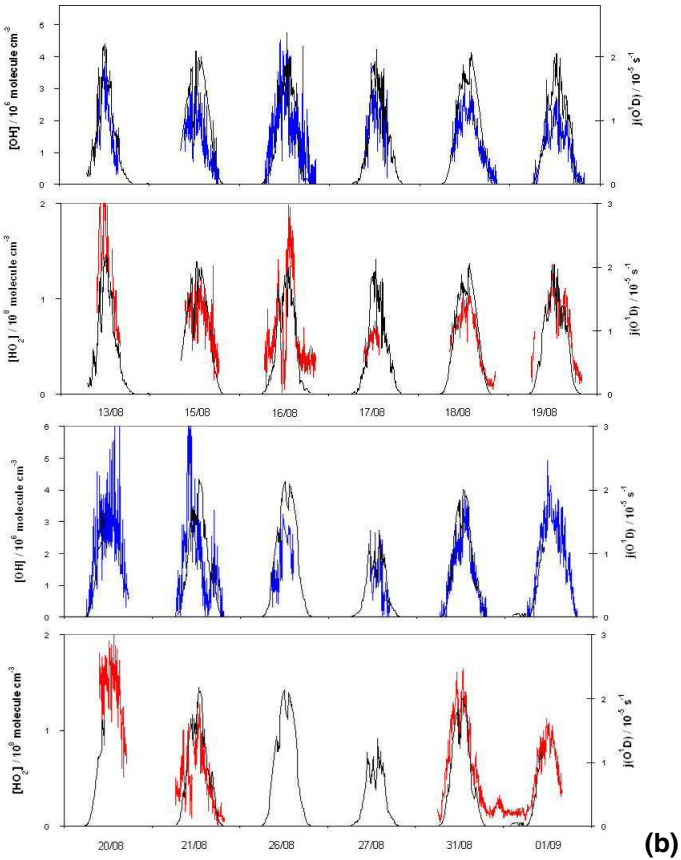

Fig. 2. Continued.

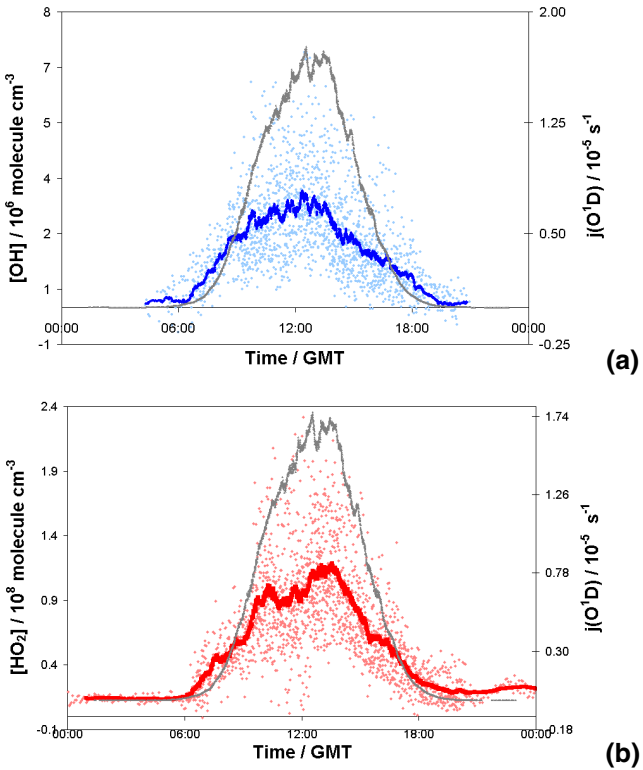

Fig. 3. **(a)** Diurnal profile of all OH data (200 s averages) for the campaign (light blue circles), together with a 40 point running mean of the OH data, (dark blue lines) and a campaign averaged $j-(O^1D)$ (grey line). **(b)** Diurnal profile of all HO_2 data (200 s averages) for the campaign (pink diamonds), together with a 40 point running mean (red line) and a campaign averaged $j-(O^1D)$ (grey line).

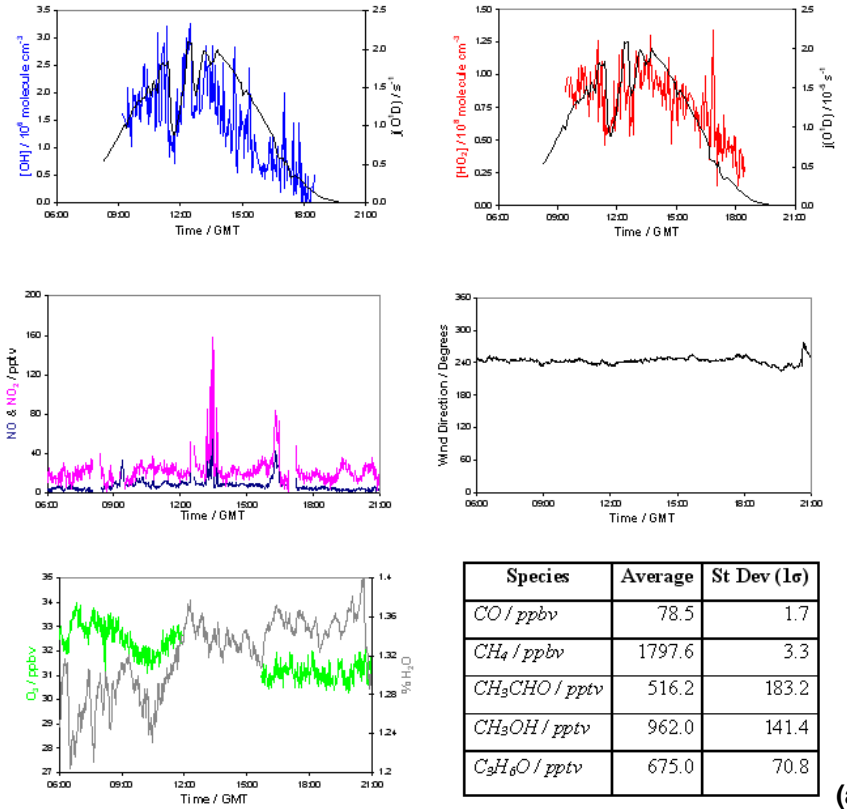

Species	Average	St Dev (1σ)
CO / ppbv	78.5	1.7
CH_4 / ppbv	1797.6	3.3
CH_3CHO / pptv	516.2	183.2
CH_3OH / pptv	962.0	141.4
C_3H_6O / pptv	675.0	70.8

(a)

Fig. 4. Time-series and a table of other relevant information are shown for the four case study days described in Sect. 4.2 of the text; **(a)** 15 August, **(b)** 16 August, **(c)** 18 August and **(d)** 21 August. The top 2 panels show 200 s averaged OH (blue) and HO_2 (red) (recorded in a 5 min cycle which includes background measurements) with 5 min average $j-(O^1D)$ (black). The middle panels show NO (navy blue) and NO_2 (pink), and wind direction (black). The bottom panels show O_3 (green) and H_2O (grey), and a table of the daily average CO, CH_4, acetaldehyde, methanol and acetone concentrations together with their respective 1σ variability.

ACPD
5, 12403–12464, 2005

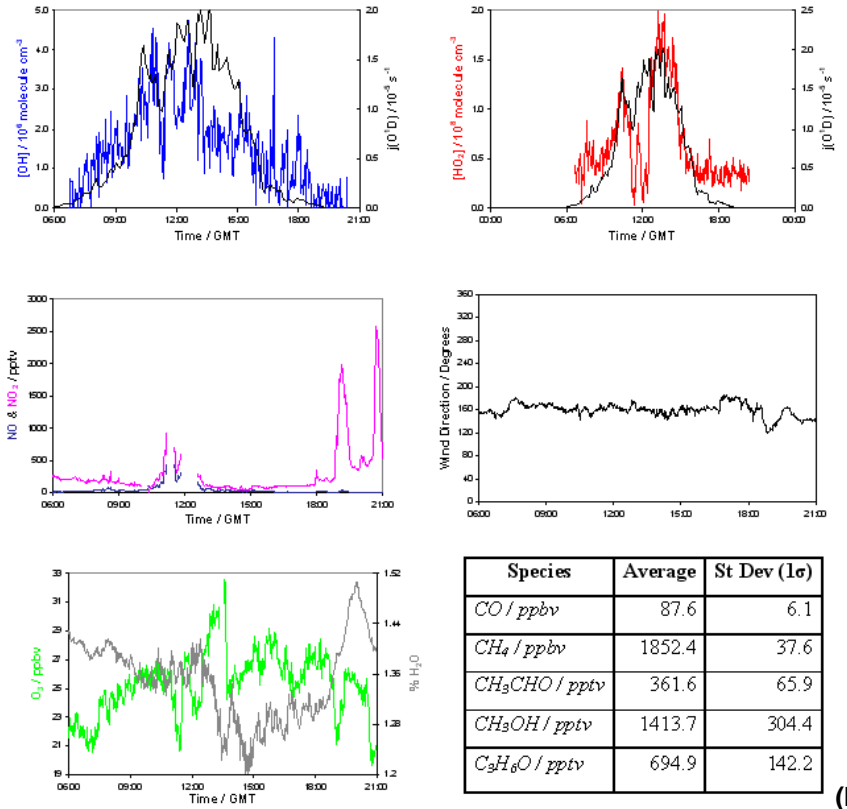

Species	Average	St Dev (1σ)
CO / ppbv	87.6	6.1
CH_4 / ppbv	1852.4	37.6
CH_3CHO / pptv	361.6	65.9
CH_3OH / pptv	1413.7	304.4
C_3H_6O / pptv	694.9	142.2

(b)

Fig. 4. Continued.

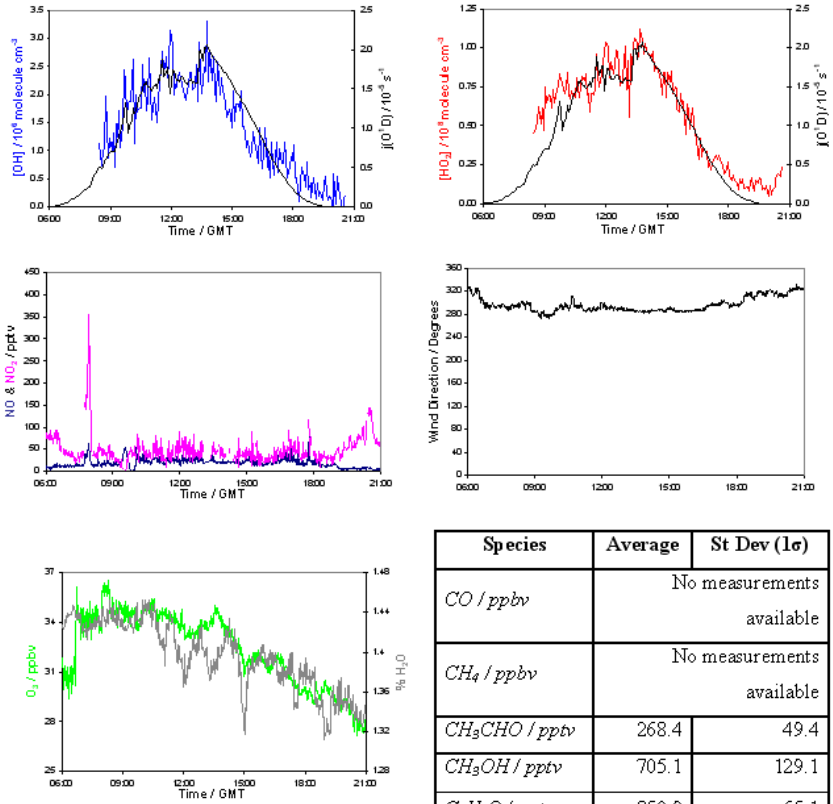

Species	Average	St Dev (1σ)
CO / ppbv	No measurements available	
CH_4 / ppbv	No measurements available	
CH_3CHO / pptv	268.4	49.4
CH_3OH / pptv	705.1	129.1
C_3H_6O / pptv	850.9	65.1

(c)

Fig. 4. Continued.

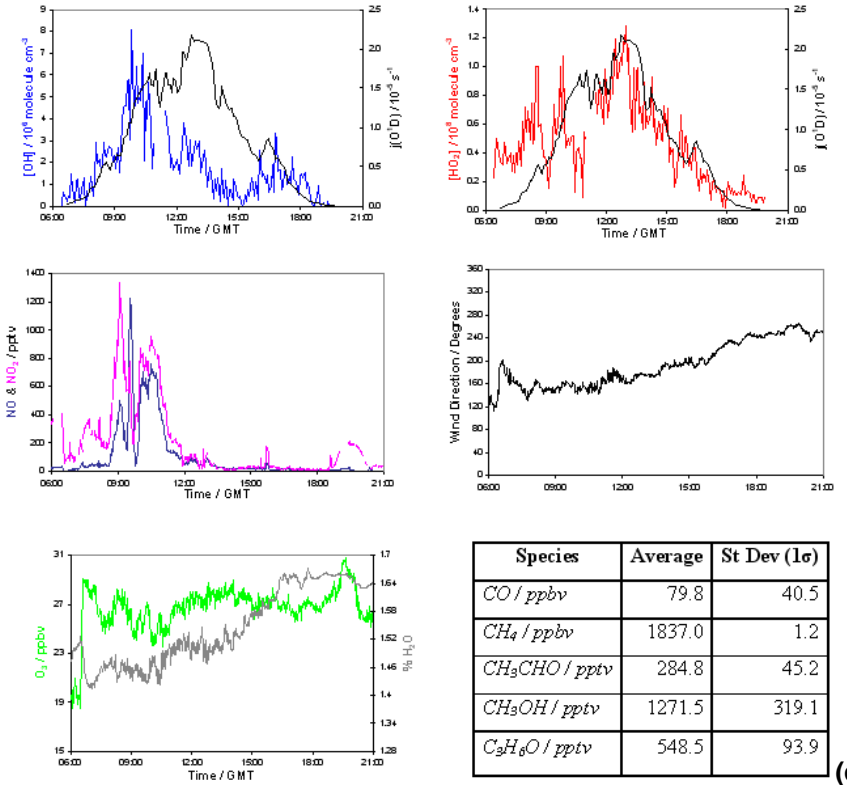

Species	Average	St Dev (1σ)
CO / ppbv	79.8	40.5
CH_4 / ppbv	1837.0	1.2
CH_3CHO / pptv	284.8	45.2
CH_3OH / pptv	1271.5	319.1
C_3H_6O / pptv	548.5	93.9

(d)

Fig. 4. Continued.

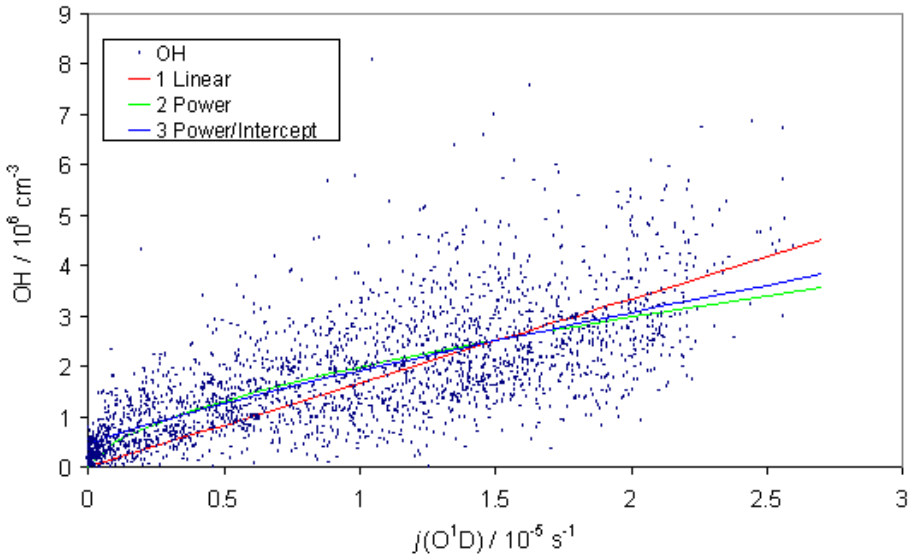

Fig. 5. Measured OH data from the NAMBLEX campaign plotted against $j-(O^1D)$ (measured by a spectral radiometer), together with fits to three versions of Eq. (10): (1) Linear (red line), (2) Power (green line) and (3) Power with intercept (blue line). See text for details.

ACPD
5, 12403–12464, 2005

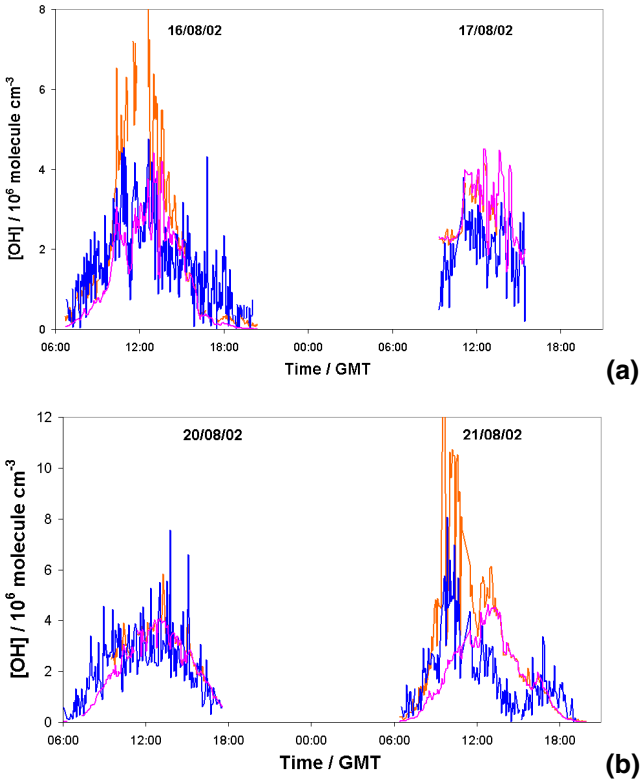

Fig. 6. Diurnal profiles of measured OH (blue line), OH calculated using the simple steady state expression Eq. (4), which includes primary production from O_3 photolysis; and loss by reaction of CO and CH_4 only (pink line), and OH calculated by a more complex steady state expression (Eq. (11)), which also includes HO_2+NO and HO_2+O_3 as OH sources, and also OH loss by reaction with *o*-VOCs (orange line) for representative 2-day periods: **(a)** 16–17 August **(b)** 20–21 August.

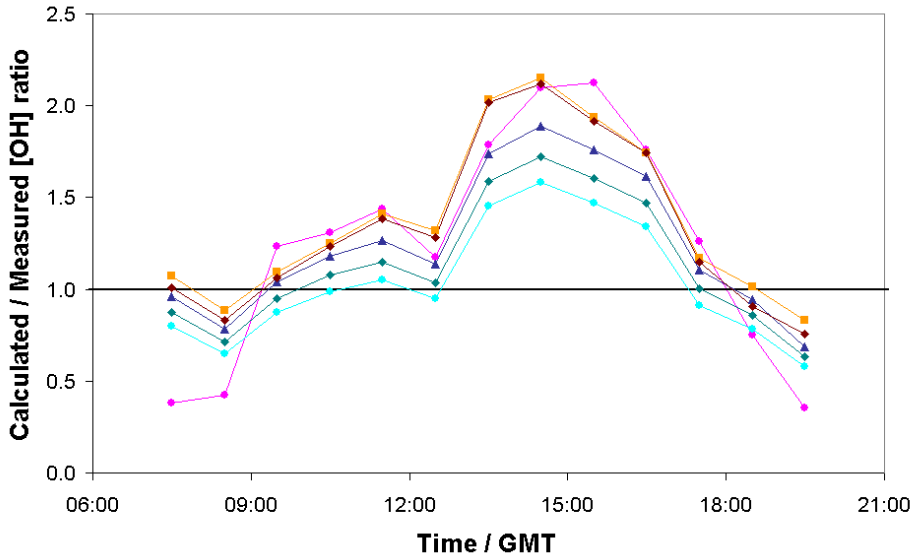

Fig. 7. Campaign averaged diurnal of the hourly average calculated/measured [OH] ratio for Eq. (4) (pink circles), Eq. (11) (orange squares), Eq. (11) including loss of OH to NO_2 (brown diamonds), Eq. (11) including loss of OH to NO_2 and HCHO (navy blue triangles), Eq. (12) which includes all of the above and also reaction with non-methane hydrocarbons (light blue circles), and Eq. (12) but excluding isoprene and DMS (green diamonds). The graph is constructed from 522×200 s averaged data points taken on 8 days between 10 and 21 August when all co-reactant data were available. Uncertainties are omitted for clarity. The mean calculated/measured OH ratios for all calculations are summarised in Table 3.

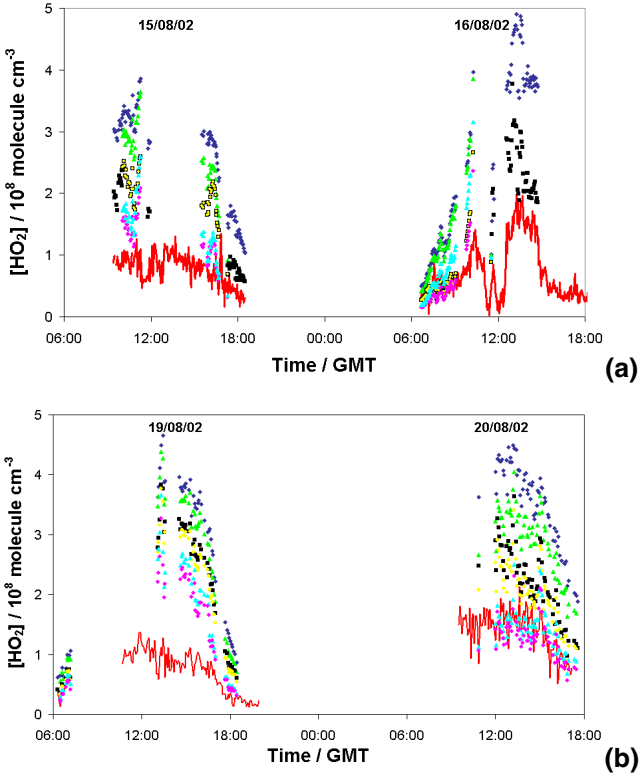

Fig. 8. Diurnal profiles of measured HO_2 (red line), and steady-state calculated HO_2 derived using Eq. (5) (navy blue diamonds) and several modifications which also include: loss by reaction of HO_2 with measured IO (green triangles), loss by reaction of HO_2 with measured IO×10 (light blue triangles), uptake of HO_2 onto aerosol (black squares), both loss of HO_2 by reaction with IO and by uptake onto aerosol (yellow circles with or without black border) and both loss of HO_2 by reaction with IO×10 and uptake onto aerosols (pink circles). The data shown are from **(a)** 15–16 August **(b)** and 19–20 August. It was not possible to calculate HO_2 between 11:57 and 15:26 GMT on the 15 August as O_3 data adjacent to the FAGE instrument were not available.

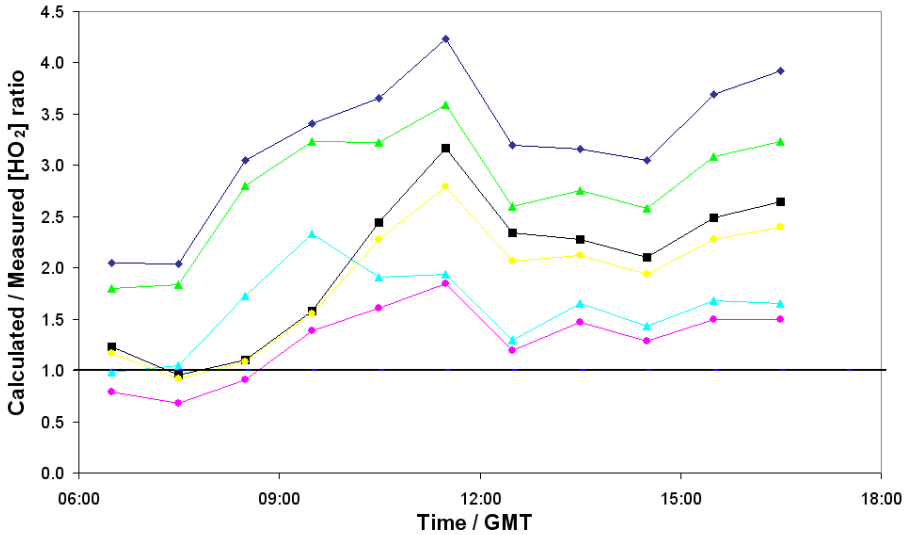

Fig. 9. Campaign average of the hourly averaged calculated/measured $[HO_2]$ ratio using Eq. (5) (navy blue diamonds) and several modifications which also include: loss by reaction of HO_2 with measured IO (green triangles), loss by reaction of HO_2 with measured IO×10 (light blue triangles), uptake of HO_2 onto aerosol (black squares), both loss of HO_2 by reaction with IO and by uptake onto aerosol (yellow circles) and both loss of HO_2 by reaction with IO×10 and uptake onto aerosol (pink circles). The graph is constructed from 281×200 s averaged data points on 6 days (13, 15–16, 19–21 August) when all co-reactant data were available. Uncertainties are omitted for clarity. The mean calculated/measured HO_2 ratios for all calculations can be found in Table 4.